Majorana Qubits and Non-Abelian Physics in Quantum Dot–Based Minimal Kitaev Chains

Athanasios Tsintzis[1,*,‡] Rubén Seoane Souto[1,2,3,4,‡] Karsten Flensberg[2] Jeroen Danon[5] and Martin Leijnse[1,2,†]

[1]*Division of Solid State Physics and NanoLund, Lund University, Lund S-22100, Sweden*

[2]*Center for Quantum Devices, Niels Bohr Institute, University of Copenhagen, Copenhagen 2100, Denmark*

[3]*Departamento de Física Teórica de la Materia Condensada, Condensed Matter Physics Center (IFIMAC) and Instituto Nicolás Cabrera, Universidad Autónoma de Madrid, Madrid 28049, Spain*

[4]*Instituto de Ciencia de Materiales de Madrid (ICMM), Consejo Superior de Investigaciones Científicas (CSIC), Sor Juana Inés de la Cruz 3, Madrid 28049, Spain*

[5]*Department of Physics, Norwegian University of Science and Technology, Trondheim NO-7491, Norway*

The possibility of engineering artificial Kitaev chains in arrays of quantum dots coupled via narrow superconducting regions has emerged as an attractive way to overcome the disorder issues that complicate the realization and detection of topological superconducting phases in other platforms. Although a true topological phase would require long chains, a two-site chain realized in a double quantum dot can already be tuned to points in parameter space where it hosts zero-energy states that seem identical to the Majorana bound states that characterize a topological phase. These states have been named "poor man's Majorana bound states" (PMMs) because they lack formal topological protection. In this work, we propose a pathway for next-generation experiments on PMMs. The pathway starts with experiments to characterize a single pair of PMMs by measuring the Majorana quality and then moves on to initialization and readout of the parity of a PMM pair, which allows the measurement of quasiparticle poisoning times. The next step is to couple two PMM systems to form a qubit. We discuss measurements of the coherence time of such a qubit, as well as a test of Majorana fusion rules in the same setup. Finally, we propose and analyze three different types of braidinglike experiments that require more complex device geometries. Our conclusions are supported by calculations based on a realistic model with interacting and spinful quantum dots, as well as by simpler models to gain physical insight. Our calculations show that it is indeed possible to demonstrate non-Abelian physics in minimal two-site Kitaev chains despite the lack of a true topological phase. However, our findings also reveal that doing so requires some extra care, appropriately modified protocols, and awareness of the details of this particular platform.

I. INTRODUCTION

Majorana bound states (MBSs) [1–5] are zero-energy excitations described by Hermitian operators. They have been predicted to exhibit exciting new physics, such as non-Abelian and nonlocal properties, which could potentially be harnessed in topological quantum computation

*atsintzis@gmail.com

†martin.leijnse@ftf.lth.se

‡These authors contributed equally to this work.

[6–9]. A simple theoretical model hosting MBSs is the Kitaev chain, a tight-binding model of a spinless p-wave topological superconductor [10]. By now, there have been many theoretical proposals (for a few examples, see Refs. [11–17]) and substantial experimental efforts (for a few examples, see Refs. [16,18–28]) aiming at creating and detecting MBSs in various systems for which the Kitaev chain is an adequate low-energy description. Despite experiments showing signatures expected for MBSs in tunneling spectroscopy, the possible emergence of non-topological Andreev bound states (ABSs) due to disorder [29–40] generally makes the interpretation challenging. Measurements of non-Abelian and nonlocal physics would constitute much stronger evidence of topological MBSs but still seem beyond experimental reach, with measurements of lifetimes or coherence properties of MBS

candidates still lacking (unlike for nontopological ABSs [41–44]).

One way to remedy the effects of disorder and material imperfections is to create a Kitaev chain with an array of quantum dots (QDs) coupled via superconducting segments [45–47]. Although long chains are needed to reach a true topological phase, a minimal Kitaev chain with only two QDs separated by a superconductor can already host states similar to MBSs [46]. These states have been called poor man's MBSs (PMMs) because they only appear in fine-tuned points (sweet spots) of the parameter space and thus lack topological protection. However, PMMs should, in principle, share all of the exotic properties of topological MBSs, including the nonlocal and non-Abelian properties.

In the simplest QD-based two-site Kitaev chain model [46], two spin-polarized QDs are coupled via two processes that involve the superconducting segment, namely, elastic cotunneling (ECT) and crossed Andreev reflection (CAR). The sweet spot where PMMs appear is found for equal strengths of CAR and ECT and QD orbitals tuned to zero energy (the middle of the superconducting gap). Since CAR is suppressed for parallel QD spins [48–51] while ECT is suppressed for antiparallel spins, Ref. [46] has suggested controlling the angle between the QD spins to fine-tune the system to the sweet spot. However, controlling the angle between the QD spins is not straightforward in practice. Another problem with this spinless model is that the QDs in a real system will never be completely spin polarized and the charging energy in the QDs will also play a role. It is thus fair to wonder whether and how PMMs would emerge in a system of partly spin-polarized and interacting QDs.

An alternative approach to control the relative magnitudes of ECT and CAR without the need to fine-tune the angle between the QD spins has been suggested in Ref. [52]. If the two QDs couple via an ABS inside the superconductor, quantum interference between different tunneling processes causes both CAR and ECT to depend on the energy of the ABS but in different ways. Thus, all that is needed to reach the PMM sweet spot is a global magnetic field together with spin-orbit coupling and control of the ABS energy.

The effects of interactions, finite Zeeman splittings, and strong coupling to the ABS have been studied in Ref. [53]. Under these realistic conditions, although there are still exact degeneracies between ground states with even and odd electron-number parity, these are not necessarily associated with PMMs and there are no points in parameter space where these degeneracies are associated with excitations that are identical to true MBSs. This necessitates the introduction of a Majorana quality measure that ideally could be accessed in experiment. One such measure is the Majorana polarization (MP) [54–56]. It has been shown in Ref. [53] that it is indeed possible to realize PMMs that are close to true MBSs, as indicated by close-to-ideal MP, but

the requirements on the parameters for doing so are nontrivial and it is also possible to end up with low-quality PMMs. Furthermore, it is not clear what is actually needed in terms of PMM quality to be able to explore nonlocal and non-Abelian physics.

Recently, a series of pioneering experiments [57–63] have demonstrated a high degree of control of the ECT and CAR magnitudes and transport-spectroscopy results that seem to be compatible with the analyses of Refs. [52,53]. In particular, Ref [58] has shown both local and nonlocal tunnel spectroscopy data that seem fully consistent with PMMs. Therefore, it appears to us that the time has now come to move on to the next generation of Majorana experiments based on PMMs.

The purpose of this paper is to sketch a pathway for this next generation of Majorana experiments, which has the demonstration of non-Abelian physics as its end destination. Before going into the details, we start with a short overview of the different experiments that we propose in this paper. We first give a brief introduction to the underlying physics and general goal of each experiment, before discussing the special problems and possibilities offered by performing them with PMMs in the QD platform.

A. Majorana quality assessment

Most simple measurements, such as local spectroscopy, cannot unambiguously distinguish between MBSs and the (nontopological) ABSs that can appear because of disorder and/or smooth potential variations [29–31,33–40,64]. In fact, one can argue that in a finite and disordered system, there is no fundamental difference between these two types of states, because a zero-energy ABS can be decomposed into two MBSs. What we call a MBS is then an ABS that decomposes into two spatially separated MBSs, such that a local experimental probe only interacts with one of them. In the ABS limit, on the other hand, the two MBSs are localized in the same region in space and any experimental probe will couple to both of them. Clearly, there is a gray zone in between these two limits where we have partially separated MBSs [37,39,65–70]. Whether it is possible to carry out nonlocal and non-Abelian operations in this regime will depend on the details and time scales of the experimental protocol. It is therefore desirable to have a measure of Majorana quality. However, it is not clear what the best-quality measure is; this will, in general, depend on for what experiment one wants to assess the Majorana quality. In this work, we will mostly use the MP [54–56] (Sec. III) as a local Majorana quality measure and we will show how it affects protocols aiming to measure nonlocal and non-Abelian properties in our PMM setup.

Compared with local spectroscopy, nonlocal tunnel spectroscopy allows us to extract more information about a bound state [27,58,71–76]. In a slightly more complicated

setup where a QD is tunnel coupled to the part of the (possibly) topological system in which a zero-energy state is localized, it is possible to estimate the MBS localization [22,77,78]. If the QD level is tuned to zero energy, it interacts with the zero-energy state. If the zero-energy state is a single isolated MBS, the QD-MBS hybridization leaves a single zero-energy state, while coupling to a second MBS (the ABS limit) results in a splitting. The spectrum can be measured by a single tunnel probe coupled to the QD. In this work, we investigate this type of spectroscopy in the PMM setup in Sec. IV B, which requires coupling a third QD to the double QD hosting the PMMs.

B. Majorana initialization and readout

Two MBSs form a single fermionic state. With no other low-energy states or excited quasiparticles, the occupation of this state (empty or full) correlates directly with the parity of the total electron number (even or odd). For a truly topological system with perfectly separated MBSs, two things hold: the even and odd ground states are perfectly degenerate (i.e., there is a fermionic state at zero energy) and no local measurement can read out the occupation of that state. Different ways have been proposed to initialize and read out the state by controlled breaking of the topological protection (see, e.g., Refs. [79–87]). In this work, we will show in Sec. V that the lack of topological protection of the PMMs is not only a bug but also a feature that allows for easy initialization and readout. We will also discuss how to measure the lifetime of such a state, which will be the limiting factor for the relaxation time of a PMM qubit. Such experiments will require coupling one of the QDs in the PMM setup to, e.g., a charge detector [88–92] or to a circuit measuring the quantum capacitance [93–95].

C. Majorana qubits

Because the state encoded in a pair of MBSs corresponds to the parity of the electron number, which is a conserved quantity, the minimal way to encode a useful qubit is in the two-level subspace spanned by the state of four MBSs with fixed total parity [2,3,7,96]. Arbitrary (unprotected) single-qubit rotations can be performed by introducing an energy associated with the occupation of the fermionic state encoded in different MBS pairs. Such controllable MBS couplings can, e.g., be based on direct overlap of MBS wave functions [14,79,97] or Coulomb interactions [80–82]. In Secs. VI A and VI B, we will discuss how to realize PMM qubits by coupling two PMM systems, either by a direct coupling between one QD in each system or by a coupling via a superconducting region. We calculate the spectrum as a function of this coupling, show how this crucially depends on the MP, and discuss the effects on single-qubit gates. This setup also allows measurements of both relaxation and coherence times. These measurements will be a benchmark on

how well-protected these nontopological MBSs actually are, which is crucial information to judge the feasibility of the non-Abelian experiments to follow.

D. Majorana fusion

The process of bringing together non-Abelian anyons to measure their joint quantum state is known as fusion and the fusion rules [6] describe the possible outcomes of such a measurement. MBSs are a realization of so-called Ising anyons [6], for which the fusion rules state that pairs can either annihilate (the measurement outcome gives an empty fermionic state in the language used above) or combine into a regular fermion (the measurement outcome gives a filled fermionic state). The simplest nontrivial experimental test of this physics requires four MBSs, where one configuration of pairings is chosen for intialization and then a different pairing is chosen for readout [81,82,98–103].

The fusion rules encode the possible measurement outcomes. In this work, we briefly discuss the fusion of PMMs in interacting QDs in Sec. VI C in a protocol similar to another recent proposal [103], requiring the same setup and control capabilities as in the qubit experiments in Sec. VI B. Although fusion of PMMs indeed seems experimentally feasible, it is not sensitive to the Majorana quality [98] and we show that the result is independent of the MP as long as one can fine-tune to a point at which the uncoupled PMM systems exhibit a perfect even-odd degeneracy.

E. Non-Abelian operations and braiding

The true hallmark feature of non-Abelian anyons is that the result of particle exchange (braiding) is described by non-Abelian representations of the braid group [6], such that the order of exchange operations matters. The robustness of the result of a braid operation—for a true topological system, it depends only on which particles are exchanged, not on the details of the exchange—is the foundational property of topological quantum computing schemes [6,7,9,85]. It might be possible to measure the non-Abelian exchange properties of MBSs by actual physical exchange of MBSs [79,104] and there are recent proposals for doing so in QD-based Kitaev chains [105]. However, most recent proposals in different superconductor-semiconductor hybrid platforms rely instead on sequences of operations that can be proven to be mathematically equivalent to braiding, including controlled additions and removal of single electrons (which we will refer to as charge-transfer-based non-Abelian operations) [83,106,107], sequences of measurements of MBS pairs (measurement-based braiding) [84,85,108], and cyclic tuning of hybridization between different MBSs (hybridization-induced braiding) [14,80–82,98,109,110].
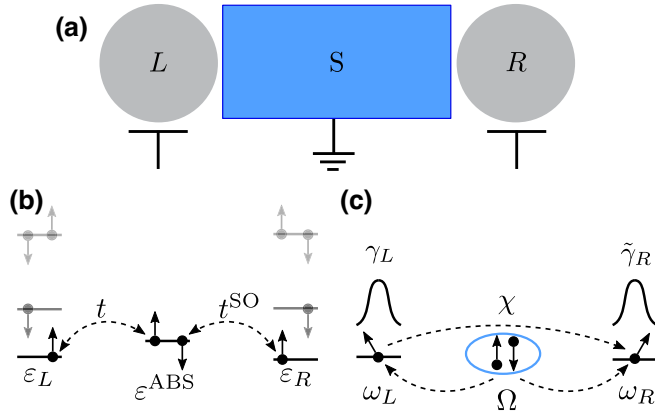
FIG. 1. (a) A sketch of a PMM system, with two QDs coupled via a grounded superconductor. We will later consider setups in which one or both QDs couple to normal-metal leads, charge detectors, or additional PMM systems. (b) The energy-level diagram, showing the orbitals of the individual QDs and the ABS, as well as different tunnel processes connecting the QDs and the ABS. (c) A sketch of the spinless model, where QDs L and R are coupled via ECT and CAR. The Majorana operators γ_L and $\tilde{\gamma}_R$ describe the degenerate ground state when the system is tuned to a sweet spot.

In Sec. VII, we propose, analyze, and numerically test setups and protocols for all these three types of non-Abelian protocols, each of which come with different advantages and difficulties. They all build directly on the ingredients introduced in earlier sections, although more complex geometries are needed. Our focus here is on deviations from the ideal MBS braiding results induced by the imperfect MBS quality (signaled by the MP), which is unavoidable in a realistic PMM system. We find that, in contrast to the fusion protocol, although the result of a braiding operation is in general a non-Abelian operation, it only comes close to the topological MBS result for close-to-ideal MP. Thus, we conclude that a braiding experiment will be the real test of the similarities between PMMs and true topological MBSs.

II. MAJORANA BOUND STATES IN A DOUBLE QUANTUM DOT

Here, we introduce and discuss the basic system with two QDs coupled via a superconductor as sketched in Fig. 1(a) and briefly explain how PMMs appear in this system. In later sections of the paper, we will add additional ingredients to this basic setup. Throughout the paper, we set $e = \hbar = k_B = 1$.

A. Model with interacting spinful quantum dots

We will base most of our conclusions in this work on a model that includes spin and Coulomb interactions on the

QDs and allows for strong coupling to the superconductor [53]. Figure 1(b) shows a sketch of the states of the two QDs and their couplings to the superconductor, which we describe by the Hamiltonian $H = H_{\mathrm{QDs}} + H_{\mathrm{ABS}} + H_{\mathrm{T}}$. Here, the two QDs are described by

$$H_{\mathrm{QDs}} = \sum_{\sigma,j} \varepsilon_{j\sigma} n_{j\sigma} + \sum_j U_j n_{j\uparrow} n_{j\downarrow}, \qquad (1)$$

where $d_{j\sigma}^\dagger$ creates an electron with spin $\sigma = \uparrow, \downarrow$ in QD $j = L, R$ with occupation $n_{j\sigma} = d_{j\sigma}^\dagger d_{j\sigma}$, single-particle orbital energy $\varepsilon_{j\sigma}$, which includes the Zeeman energy $\varepsilon_{j\uparrow/\downarrow} = \varepsilon_j \pm E_{Zj}/2$, and Coulomb charging energy U_j. We assume that the orbital spacing is large enough that we can restrict the model to a single orbital on each QD.

The coupling between the QDs via the superconductor is assumed to be dominated by a discrete ABS. This might be a subgap state in a narrow region of proximitized semiconductor [52,57–60,62,63] or a third QD that is in turn strongly coupled to a bulk superconductor [53]. For definiteness, we choose

$$H_{\mathrm{ABS}} = \sum_\sigma \varepsilon_\sigma^{\mathrm{ABS}} n_\sigma^{\mathrm{ABS}} + \Delta c_\uparrow^\dagger c_\downarrow^\dagger + \Delta^* c_\downarrow c_\uparrow, \qquad (2)$$

where $c_\sigma^\dagger$ is the electron creation operator in the superconductor, $n_\sigma^{\mathrm{ABS}} = c_\sigma^\dagger c_\sigma$, and $\varepsilon_{\uparrow/\downarrow}^{\mathrm{ABS}} = \varepsilon^{\mathrm{ABS}} \pm E_Z^{\mathrm{ABS}}/2$. We neglect on-site Coulomb interactions for the ABS, motivated by the assumption that the central region of the PMM system is strongly coupled to a grounded superconductor that screens its charge. This is the case in the experiments described in Refs. [57–60,62,63]. We note that PMM sweet spots can also be found when the central region features a charging energy, as discussed in Ref. [53]. We, for now, assume Δ to be real, but will discuss the general case later when considering setups with more than one superconductor.

The coupling between the QDs and the ABS is described by

$$H_{\mathrm{T}} = \sum_\sigma s_\sigma \left[t_L^{\mathrm{SO}} d_{L\sigma}^\dagger c_{\bar{\sigma}} + t_R^{\mathrm{SO}} c_\sigma^\dagger d_{R\bar{\sigma}} \right]$$
$$+ \sum_{\sigma,j} t_j d_{j\sigma}^\dagger c_\sigma + \mathrm{h.c.} \qquad (3)$$

Here, $s_{\uparrow,\downarrow} = \pm 1$, t_j is the amplitude for spin-conserving tunneling between QD j and the ABS and t_j^{SO} is the amplitude for the corresponding spin-flip tunneling process that results from a spin-orbit interaction with spin-orbit field $\mathbf{B}_{\mathrm{SO}}$ along the y axis, perpendicular to the external Zeeman field $\mathbf{B}$ (cf. Ref. [111]).

To describe experiments in which the PMM system is coupled to external normal-metal source and drain leads

that allow for (local and nonlocal) conductance measurements, we add the following terms to our Hamiltonian to describe the electronic states in lead r and their couplings to the level on QD j:

$$H_{rj}^{\text{res}} = \sum_{k\sigma} \varepsilon_{rk\sigma} c_{rk\sigma}^\dagger c_{rk\sigma} + \left[\sum_{k\sigma} t_{rjk\sigma} d_{j\sigma}^\dagger c_{rk\sigma} + \text{h.c.} \right]. \quad (4)$$

Here, $\varepsilon_{rk\sigma}$ is the energy of an electron in level k with spin σ in lead r (relative to the Fermi level) and $t_{rjk\sigma}$ parametrizes the coupling strength of that level to the localized state on the QD to which the lead is coupled (for simplicity, we only include spin-conserving tunneling). For example, for the case of a transport setup where QD L is coupled to a source and QD R to a drain contact, we would add $H_{SL}^{\text{res}} + H_{DR}^{\text{res}}$ to the Hamiltonian. For our numerical simulations of transport experiments, we always focus on the regime where the tunnel coupling to the leads is the smallest energy scale and solve for the current with a rate-equation approach [112].

B. Spinless model

When $|\varepsilon_{j\downarrow}|, |t_j|, |t_j^{\text{SO}}|, |E_Z^{\text{ABS}}| \ll |\Delta|, |E_{ZL,R}|$, one can neglect occupation of the excited spin state and treat the couplings between QDs L and R via the ABS in second-order perturbation theory. The model in Eqs. (1)–(3) then reduces to the effectively spinless and noninteracting model of Ref. [46], sketched in Fig. 1(c) and described by

$$H^{\text{spinless}} = \sum_j \omega_j n_j + \left[\chi\, d_L^\dagger d_R + \Omega\, d_L^\dagger d_R^\dagger + \text{h.c.} \right]. \quad (5)$$

The QD orbital energy $\omega_j \approx \varepsilon_{j\downarrow}$ but is renormalized by the couplings to the ABS, while χ and Ω are the amplitudes for ECT and CAR between QDs L and R, resulting from second-order perturbation theory in t_j and t_j^{SO}. Similarly to the spinful interacting case, for a single PMM system, any phase of Ω can be gauged away. We thus take Ω to be real without loss of generality.

We will sometimes use the spinless model in Eq. (5) to gain intuitive understanding or analytical results. However, it might not be experimentally possible to reach a regime where mapping onto the spinless model is appropriate and it might not even be desirable, because $|t_j|, |t_j^{\text{SO}}| \ll |\Delta|$ implies a small gap to excited states. Importantly, it has been shown in Ref. [53] that one can also reach a regime with high-quality PMMs in the regime where such a mapping is not appropriate.

In the spinless model in Eq. (5), there is a sweet spot with a degeneracy between the lowest-energy states with even and odd fermion-number parity, which is associated with having one perfect PMM localized on each QD, denoted by $\gamma_L = d_L^\dagger + d_L$ and $\tilde{\gamma}_R = i(d_R^\dagger - d_R)$ in Fig. 1(c). This sweet spot occurs when the spin-polarized QD

orbitals are at zero energy, $\omega_L = \omega_R = 0$ (i.e., they are aligned with the chemical potential of the superconductor coupling them) and when the amplitudes for CAR and ECT are equal, $\Omega = \chi$. Ref. [46] has proposed tuning the amplitudes for CAR and ECT through the angle between the noncollinearly polarized QD spins. In the spinful model, both of these processes are possible because of the spin-orbit coupling and control of the relative amplitudes can be achieved by controlling the energy of the ABS coupling the QDs because of an interference effect described in Ref. [52] and studied experimentally in Ref. [60] (see also Ref. [53]).

Away from the sweet spot, the splitting between the lowest even and odd states can become finite and the corresponding fermionic mode cannot always be split up into two nonoverlapping PMMs. The effect of tuning away from the sweet spot can be understood in a more quantitative way by performing a Bogoliubov transformation to write Eq. (5) as

$$H^{\text{spinless}} = \frac{1}{2}\left[\sqrt{\omega_+^2 + 4\Omega^2} - \sqrt{\omega_-^2 + 4\chi^2} \right] f_-^\dagger f_-$$
$$+ \frac{1}{2}\left[\sqrt{\omega_+^2 + 4\Omega^2} + \sqrt{\omega_-^2 + 4\chi^2} \right] f_+^\dagger f_+, \quad (6)$$

up to a constant term, where $\omega_\pm = \omega_L \pm \omega_R$ and $f_\pm^\dagger$ creates a fermion in the excited (ground) state. In terms of the Majorana operators we defined before, we can write

$$f_- = \frac{1}{2}\sin(\varphi_+)\gamma_L + \frac{i}{2}\sin(\varphi_-)\tilde{\gamma}_L$$
$$- \frac{1}{2}\cos(\varphi_+)\gamma_R - \frac{i}{2}\cos(\varphi_-)\tilde{\gamma}_R, \quad (7)$$

where $\varphi_\pm = [\arctan(2\chi/\omega_-) \pm \arctan(2\Omega/\omega_+)]/2$ and we have introduced the two additional Majorana operators $\gamma_R = d_R^\dagger + d_R$ and $\tilde{\gamma}_L = i(d_L^\dagger - d_L)$. We note that the two arctan functions are defined such that they yield an angle in the range $(0, \pi)$. This definition is crucial for obtaining correct results.

We see that when $\omega_L = \omega_R = 0$, we have $\varphi_+ = \pi/2$ and $\varphi_- = 0$ and thus $f_- = (\gamma_L - i\tilde{\gamma}_R)/2$, i.e., the lowest fermionic mode separates into two well-localized PMMs on the two QDs. However, this does not imply that the lowest odd and even states (corresponding to having the mode f_- occupied or unoccupied) must be degenerate; see Eq. (6).

C. Low-energy model

We also introduce an even simpler low-energy model, only including a single fermionic mode with energy ξ:

$$H^{\text{lowE}} = \frac{i}{2}\xi\gamma\tilde{\gamma}. \quad (8)$$

We choose the operators such that for well-localized PMMs, γ has no weight on QD R, while $\tilde{\gamma}$ has no weight on QD L. In general, we let $\zeta \leq 1$ denote the relative amplitude of $\tilde{\gamma}$ on QD L, normalized by the amplitude of γ on QD L. In the same way, we let $\tilde{\zeta} \leq 1$ denote the amplitude of γ on QD R, normalized by the amplitude of $\tilde{\gamma}$ on QD R. Then, $\zeta = 1$ ($\tilde{\zeta} = 1$) corresponds to a normal fermion on QD L (R), while $\zeta = 0$ ($\tilde{\zeta} = 0$) corresponds to a single PMM on QD L (R).

The model in Eq. (8) can be seen as a low-energy approximation to both the spinful model (Sec. II A) and the spinless model (Sec. II B). In the latter case, we define $\gamma = f_-^\dagger + f_- = \sin(\varphi_+)\gamma_L - \cos(\varphi_+)\gamma_R$ and $\tilde{\gamma} = i(f_-^\dagger - f_-) = -\cos(\varphi_-)\tilde{\gamma}_R + \sin(\varphi_-)\tilde{\gamma}_L$ and ξ is the energy of the fermion annihilated by f_- [see Eq. (6)]. This allows us to write explicitly $\zeta = \sin(\varphi_-)/\sin(\varphi_+)$ and $\tilde{\zeta} = \cos(\varphi_+)/\cos(\varphi_-)$.

We will use generalizations of Eq. (8) to two- and three-PMM systems in Secs. VI and VII to gain intuitive understanding and compare with the physics of true topological MBSs.

III. MEASURES FOR MAJORANA QUALITY

When there is no clear separation between energy scales, the model in Eqs. (1)–(3) does not reduce to the spinless model given in Eq. (5). In this case, both spin states on the QDs must be accounted for, the QD charging energy becomes important, and we cannot project out the occupation of the ABS. Nonetheless, it has been shown in Ref. [53] that for a wide range of parameters, by varying $\varepsilon_{j\sigma}$ and $\varepsilon_\sigma^{\text{ABS}}$ one finds two sweet spots associated with localized PMMs. However, unlike in the spinless model given in Eq. (5), these PMMs are never perfect, even at the sweet spot where the degeneracy is (almost completely) robust to detuning of individual QD levels. In Ref. [53], the PMM quality (or closeness to perfect MBSs) has been quantified through the MP defined by

$$M_j = \frac{\sum_\sigma \left(w_{j\sigma}^2 - z_{j\sigma}^2 \right)}{\sum_\sigma \left(w_{j\sigma}^2 + z_{j\sigma}^2 \right)}, \tag{9}$$

$$w_{j\sigma} = \langle o|(d_{j\sigma} + d_{j\sigma}^\dagger)|e\rangle, \tag{10}$$

$$z_{j\sigma} = \langle o|(d_{j\sigma} - d_{j\sigma}^\dagger)|e\rangle, \tag{11}$$

where $|e\rangle$ ($|o\rangle$) is the lowest-energy state with total even or odd fermion-number parity. It always holds that $-1 \leq M_j \leq 1$. It should be noted that this definition of the MP assumes real wave functions, which we can always choose, because the Hamiltonians in Eqs. (1)–(3) are real; for complex wave functions, there is a phase degree of freedom in the definition of $w_{j\sigma}$ and $z_{j\sigma}$ which requires some extra care.

The MP given in Eq. (9) can be calculated anywhere in parameter space but we would only really call the states PMMs if we had a combination of high (close-to-unity) MP and a (quasi)degeneracy between the even- and odd-parity ground states. $|M_j| = 1$ means that only a single Majorana operator that switches between these even- and odd-parity ground states has any weight on QD j. In the different experiments proposed and investigated below, we will study the effects of having low MP even at the best possible sweet spot (resulting from a too low E_{Zj} and U_j [53]). We will also consider (intentional and unintentional) deviations from the sweet spot, which can break the even-odd degeneracy and/or reduce the MP.

In the spinless model described in Sec. II B, we can use Eq. (7) to find explicit expressions for the MP:

$$M_L = \frac{\sin(\varphi_+)^2 - \sin(\varphi_-)^2}{\sin(\varphi_+)^2 + \sin(\varphi_-)^2} \tag{12}$$

$$= \frac{-4\chi\Omega}{\omega_+\omega_- - \sqrt{(\omega_-^2 + 4\chi^2)(\omega_+^2 + 4\Omega^2)}} \tag{13}$$

and

$$M_R = \frac{\cos(\varphi_+)^2 - \cos(\varphi_-)^2}{\cos(\varphi_+)^2 + \cos(\varphi_-)^2} \tag{14}$$

$$= \frac{-4\chi\Omega}{\omega_+\omega_- + \sqrt{(\omega_-^2 + 4\chi^2)(\omega_+^2 + 4\Omega^2)}}. \tag{15}$$

We note that these expressions simply quantify how purely real (γ_j) or imaginary ($\tilde{\gamma}_j$) the component of the ground-state wave function on QD j is, perfect MP corresponding to $M_L = \pm 1, M_R = \mp 1$.

Within the low-energy model introduced in Sec. II C, it seems reasonable to define the MP as

$$M_L \approx \frac{1 - \zeta^2}{1 + \zeta^2}, \quad M_R \approx -\frac{1 - \tilde{\zeta}^2}{1 + \tilde{\zeta}^2}. \tag{16}$$

This clearly agrees with Eqs. (12) and (14) if we derive the low-energy model from the spinless model but we emphasize that, for relatively high MP (small ζ), Eqs. (8) and (16) hold more generally, i.e., also when the PMMs have some weight on the ABS and on the excited spin state. When investigating coupled PMM systems and braiding in Secs. VI and VII, we will see that, assuming that we have tuned the system to even-odd degeneracy, ζ and $\tilde{\zeta}$ indeed quantify how the results deviate from those expected for topological MBSs.

We emphasize that M_j is normalized to the total weight of the wave function on the QD under consideration. This suggests that one can have $|M_j| = 1$ even with only negligible average occupation of QD j. This can be clearly seen in the spinless model, where, e.g., in the limit $\omega_R \to \infty$

and $\omega_L = 0$, one finds for $\chi = \Omega$ that the even and odd ground states are the trivial states $|0\rangle$ and $d_L^\dagger|0\rangle$; however, in this case, Eqs. (13) and (15) yield $M_L = 0$ for QD L but $M_R = -1$ for the empty QD R. The quantities $M_{L,R}$ are thus not very good measures for the "Majoranaeness" of the ground-state wave function as a whole. They are, however, useful to consider when one is interested in coupling multiple PMM systems, to form qubits and perform fusion or braiding experiments. As discussed in Sec. VI A, when two PMMs are connected via two QDs, AR and BL, that have $|M_{AR}| = |M_{BL}| = 1$, the resulting coupling in the low-energy sector can be written in the form $H_{AB}^{\text{lowE}} = i\lambda_{AB}\gamma_A\gamma_B/2$; reduced weights on the coupled QDs reduce the effective coupling strength λ_{AB} but will not introduce any undesired finite-coupling matrix elements between other Majorana components of the low-energy modes.

We note that the product of the two polarizations $-M_L M_R$ or their weighted sum $|M_L - M_R|/2$ could be used as a measure for the Majorana quality of the whole PMM system, both measures reaching 1 in the ideal case.

In case one is interested in a measure that takes into account the relative weight of the mode on the outer QDs, one could also consider the quantity

$$M_{\text{G}} = \frac{1}{2}\big[\cos(\varphi_+)^2 - \cos(\varphi_-)^2\big]^2$$
$$+ \frac{1}{2}\big[\sin(\varphi_+)^2 - \sin(\varphi_-)^2\big]^2 \tag{17}$$
$$= \frac{16\chi^2\Omega^2}{(\omega_-^2 + 4\chi^2)(\omega_+^2 + 4\Omega^2)}, \tag{18}$$

written here in terms of the spinless model (one could straightforwardly construct an equivalent expression for the spinful case). This quantity satisfies $0 \leq M_{\text{G}} \leq 1$ and only reaches its maximum when $f_- = (\pm\gamma_L \mp i\tilde{\gamma}_R)/2$ or $f_- = (\mp\gamma_R \pm i\tilde{\gamma}_L)/2$, i.e., when the lowest-energy mode is a perfect PMM with all its weight on the two outer QDs. This M_{G} is thus more closely related to a global Majorana quality of the full wave function corresponding to the lowest mode. However, in the spinful model, the wave function will also have some weight on the ABS and a generalization of M_{G} will thus rarely approach 1. The same will hold for any more complex model with additional degrees of freedom. A low value of M_{G} could indicate a strong mixing of the Majorana components of the wave function but could also be merely related to a small total weight of the state on the outer QDs.

For the experiments considered in Secs. VI and VII, only the Majorana quality in the parts of the PMM system that are coupled to other components matters. This is quantified by the normalized local M_j and we therefore focus on this quantity in the following.

IV. DETECTING MAJORANA STATES

A. Tunneling spectroscopy

The most straightforward way to probe the low-energy physics in a PMM system is to connect it via tunneling barriers to metallic reservoirs, as sketched in Fig. 2(a), and perform tunneling spectroscopy. In such a setup, the full differential conductance matrix $G_{jk} = dI_j/dV_k$, with $j, k = L, R$, can be accessed by varying the voltages V_k applied to the reservoirs and monitoring the currents I_j flowing into the two sides of the PMM system. A peak in the local differential conductances G_{jj} at small bias voltage signals a degeneracy of the lowest even and odd states. Mapping out the structure of this degeneracy as a function of the QD orbital energies, which can be controlled via electrostatic gates, can provide information about the ratio of CAR and ECT and could thus serve as a guidance for tuning toward points in parameter space with large MP [53,58]. A measurement of the nonlocal differential conductances G_{LR} and G_{RL} provides additional information about the detailed structure of the bound state involved in the transport, including its "BCS charge" distribution over the two QDs [74], such that a sign change of G_{LR} and G_{RL} coinciding with the degeneracy can provide extra evidence for a bound state with high MP [58]. The nonlocal nature of MBSs can also be probed with shot-noise spectroscopy [113–119] or entropy measurements [120–124].

B. Coupling to an extra quantum dot

Another method to assess the quality of the PMMs and indirectly probe their MP is to add one extra QD to the setup and measure the conductance of the combined QD-PMM setup [see Fig. 2(b)]. While direct local tunneling spectroscopy on the bare PMM system can only reveal the presence of a low-energy state that has significant weight on one end of the system, the addition of the extra QD makes the level structure of the combined setup sensitive to the exact distribution of the state over the whole PMM part of the system, thus providing insight into the Majorana quality of the state through straightforward local conductance measurements only. In the search for MBSs in proximitized nanowires, the addition of such an extra QD has indeed yielded features in the low-energy part of the spectrum that have been interpreted as signatures of the absence or presence of low-energy modes corresponding to localized MBSs [22,77,78,125].

To investigate this setup in more detail for the PMM system, we thus add an extra QD "D" to our model, which we account for by adding to the Hamiltonian

$$H_D = \sum_\sigma \varepsilon_{D\sigma} n_{D\sigma} + U_D n_{D\uparrow} n_{D\downarrow}$$
$$+ \sum_\sigma \Big[t_D d_{D\sigma}^\dagger d_{L\sigma} + t_D^{\text{SO}} s_\sigma d_{D\sigma}^\dagger d_{L\bar\sigma} + \text{h.c.}\Big], \tag{19}$$
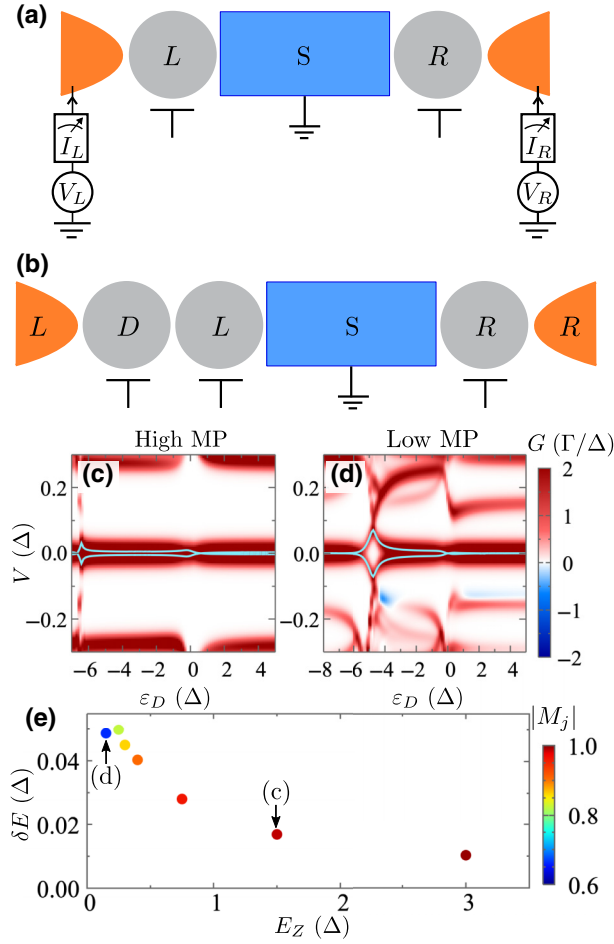
FIG. 2. (a) The transport setup that allows for measurement of the full differential conductance matrix of a PMM system, such as performed in Ref. [58]. (b) The QD-PMM system embedded in a similar transport setup as in (a). (c) The local differential conductance ($G = G_{RR}$) of the QD-PMM system for a high-MP sweet spot as a function of the bias voltage $V/2 = V_L = -V_R$ and the QD orbital energy ε_D. The solid light-blue lines show the difference between the lowest even and odd states obtained from numerical diagonalization of the spinful Hamiltonian. (d) The same as (c) but for a low-MP sweet spot. (e) The maximum splitting between the even and odd ground states when sweeping ε_D as a function of the Zeeman splitting on all the QDs, for parameters corresponding to different MP values (indicated by the dot color). In all calculations, we have used (all in units of Δ) $U_L = U_R = U_D = 5$ and $E_Z^{ABS} = 0$. All the tunnel couplings between the QDs have been chosen equal to $t_j = 0.5$ and the spin-orbit tunnel couplings are set to $t_j^{SO} = 0.1$. To change the MP, we have varied $E_{ZL,R}$ (with $E_{ZD} = E_{ZL,R}$) and adjusted ε_L, ε_R, and ε^{ABS} to find a sweet spot. In (c) (high MP, $|M_{L,R}| \approx 0.986$), we have used $E_{ZL} = E_{ZR} = E_{ZD} = 1.5$, $\varepsilon_L = \varepsilon_R = -0.154$, and $\varepsilon^{ABS} = -0.329$. In (d) (low MP, $|M_{L,R}| \approx 0.661$), we have used $E_{ZL} = E_{ZR} = E_{ZD} = 0.15$, $\varepsilon_L = \varepsilon_R = -0.306$, and $\varepsilon^{ABS} = -0.564$.

where $d_{D\sigma}^{\dagger}$ creates an electron with spin σ on the extra QD D. QD D is only tunnel coupled to QD L of the PMM system [see Fig. 2(b)] and the orbital on the QD D has the (spin-dependent) single-particle energy $\varepsilon_{D\sigma} =$

$\varepsilon_D \pm E_{ZD}/2$ and an on-site Coulomb charging energy of U_D. For simplicity, we have not included inter-QD electrostatic interaction between QDs D and L, which could in principle be significant, since they are not separated by a superconducting element that screens the interaction. We will assume here that such interactions are being screened by additional metallic components or actively compensated for in the gating of the device.

This combined QD-PMM system is then connected to a source and a drain lead, as indicated in Fig. 2(b). We include this in our model by adding the terms $H_{LD}^{res} + H_{RR}^{res}$ to the Hamiltonian [see Eq. (4)] and numerically calculate the current through the system (see Sec. II A).

Figures 2(c) and 2(d) show the calculated local differential conductance G_{RR} as a function of the symmetrically applied bias voltage $V/2 = V_L = -V_R$ and the QD detuning ε_D. We plot the conductance in units of Γ/Δ, where $\Gamma = 2\pi t_{rjk\sigma}^2 \nu_{res}$ is the tunnel rate to the reservoirs, with ν_{res} the density of states of the reservoirs, which, together with the tunnel-coupling coefficients, $t_{rjk\sigma}$, is assumed to be energy and spin independent and is set the same for the two sides of the system. Within the rate-equation approach, Γ is just a prefactor and the conductance plotted in units of Γ/Δ is independent of Γ. However, the rate equation is only valid under the assumption $\Gamma \ll T$, where we take the thermal energy to be $T = \Delta/200$. All other parameter values are specified in the caption of Fig. 2.

In all the panels, the PMM system is tuned to a sweet spot, i.e., a point in the parameter space (ε_L, ε_R, ε^{ABS}) where the lowest even and odd states are degenerate, the degeneracy is quadratically protected against deviations of $\varepsilon_{L,R}$, and the MP is maximized (cf. Ref. [53]). Figure 2(c) shows the case where the sweet spot has relatively high MP values, $|M_R| = |M_L| = 0.986$, whereas in Fig. 2(d) we have lower $|M_R| = |M_L| = 0.661$, due to a 10 times lower Zeeman splitting. The solid light-blue lines indicate the energy difference between the lowest even and odd states, found from numerically diagonalizing the spinful Hamiltonian.

Similar to the case with MBSs in nanowires [22,77,78, 125], we see that the case with high MP distinguishes itself by showing much smaller splitting of the zero-bias peak as a function of the QD level ε_D, a feature that is indeed clearly visible in the local conductance data. The intuitive picture is that if QD D only couples to a single PMM, it cannot break the ground-state degeneracy and level crossings will thus not produce significant splitting. In general, we note that the line shapes that we observe close to the level crossings strongly resemble those observed in experiments [22,78], which have been called "bowtie" and "diamond" patterns [77,125].

To corroborate the connection between the observed level splitting at the crossing and the MP of the PMM system, we show in Fig. 2(e) the maximal even-odd ground-state splitting δE around the level crossings as a function

of the Zeeman splitting on the three QDs. For each point, we have tuned the PMM system to a sweet spot, where the even and odd ground states are degenerate, the degeneracy is quadratically protected against deviations of $\varepsilon_{L,R}$, and the MP is maximal. The colors of the dots indicate the MP, which ranges from 0.661 for a Zeeman splitting of $E_Z = 0.15\,\Delta$ to 0.995 for $E_Z = 3\,\Delta$. The dependence of the MP on the Zeeman splitting is well known [53]; additionally, we see a clear correlation between the MP and the maximal δE when sweeping ε_D, with δE converging to 0 for $|M_L| = 1$.

These results clearly indicate that the addition of an extra QD can facilitate probing the Majorana quality of the low-energy states in a PMM system, using local tunneling spectroscopy only.

C. Quantum capacitance and Majorana polarization

Another method to access the Majorana quality of a PMM system could be to monitor the quantum capacitance of the lowest even and odd state with respect to one of the gate voltages that control the QD levels. In the spinless model, the even (odd) charge sector is spanned by the two basis states $|00\rangle = |0\rangle$ and $|11\rangle = d_L^\dagger d_R^\dagger |0\rangle$ ($|10\rangle = d_L^\dagger |0\rangle$ and $|01\rangle = d_R^\dagger |0\rangle$). At the sweet spot, where $\omega_L = \omega_R = 0$, the lowest even and odd eigenstates become $(|00\rangle - |11\rangle)/\sqrt{2}$ and $(|10\rangle - |01\rangle)/\sqrt{2}$, respectively, together defining a fermionic mode that is comprised of two perfect MBSs. Both of these states are equal superpositions of different charge states, which is indeed a crucial ingredient to make them indistinguishable by local charge measurements, a characteristic property related to the nonlocal nature of MBSs. However, this also implies that at the sweet spot, the charge distribution of both states is most sensitive to small changes in the on-site potentials, suggesting a local maximum in the magnitude of the quantum capacitances $C_{pj} = d^2 E_p / d\omega_j^2$, where $p = e, o$ denotes the parity of the state, and $j = L, R$.

The simplicity of the spinless model allows us to straightforwardly find analytical expressions for the capacitances,

$$C_{ej} = -\frac{2\Omega^2}{\left(\omega_+^2 + 4\Omega^2\right)^{3/2}}, \qquad (20)$$

$$C_{oj} = -\frac{2\chi^2}{\left(\omega_-^2 + 4\chi^2\right)^{3/2}}, \qquad (21)$$

which are equal for $j = L, R$ and their magnitudes are indeed both maximal at the point $\omega_{L,R} = 0$. In fact, we see that in the spinless model, there is a direct connection with M_G, which is defined in Eq. (18),

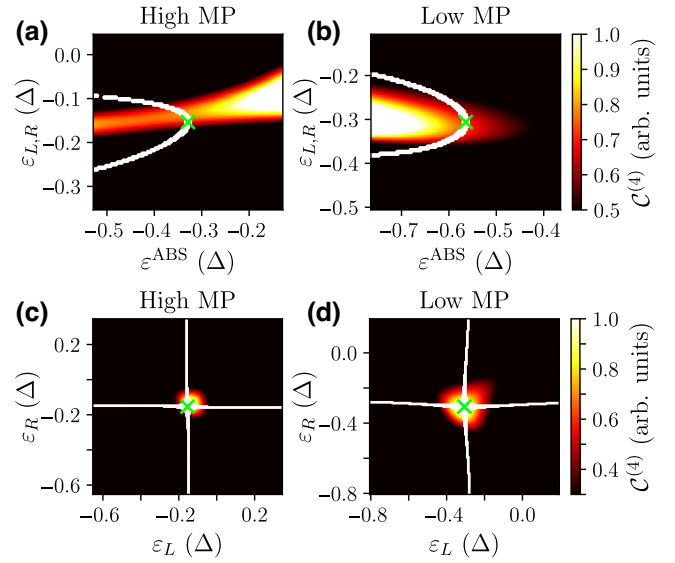$$C_{ej} C_{oj} = \frac{M_G^{3/2}}{16\chi\Omega}. \qquad (22)$$

FIG. 3. The product of the four capacitances $\mathcal{C}^{(4)}$ as a function of the gate-tunable parameters (a),(b) $\varepsilon_L = \varepsilon_R$ and ε^{ABS} or (c),(d) ε_L and ε_R. In (a) and (c), we have used the same parameters as in Fig. 2(c) and in (b) and (d), we have used the same parameters as in Fig. 2(d). The green crosses mark the locations of the local sweet spot, where the even-odd splitting vanishes, the degeneracy is quadratically protected against deviations of $\varepsilon_{L,R}$, and the local $M_{L,R}$ are maximized. The white lines indicate the trajectory of the ground-state degeneracy in parameter space (we plot all points with even-odd energy splitting below a threshold value in white).

A local maximum of $C_{ej} C_{oj}$ as a function of the tuning parameters can thus be interpreted as a signal of high MP.

To find the sweet spot in an experiment, one could first find the manifold in parameter space that yields a vanishing even-odd splitting, using local tunneling spectroscopy. After that, one could monitor the capacitance of the QDs of the PMM system, via rf reflectometry (see, e.g., Ref. [93–95]), while allowing for tunneling events that change the parity of the system, or just rely on randomly occurring quasiparticle poisoning processes to switch between the even and odd ground states. From the telegraph signal measured, one can extract a measure for both C_{ej} and C_{oj}. The product $C_{ej} C_{oj}$ is expected to have a maximum at the Majorana sweet spot for zero energy splitting, which can be used to tune the energy of the QDs.

We now explore the extent to which this relationship holds in the spinful interacting model, with finite on-site Zeeman splittings. The capacitances are now defined as $C_{pj} = d^2 E_p / d\varepsilon_j^2$ and are in general no longer symmetric in $j = L, R$. In Fig. 3, we thus plot the product of the four capacitances $\mathcal{C}^{(4)} = C_{eL} C_{eR} C_{oL} C_{oR}$ and assess the correlation between local maxima of this quantity and the location of the sweet spot. Figures 3(a) and 3(b) show $\mathcal{C}^{(4)}$ as a function of $\varepsilon_L = \varepsilon_R$ and ε^{ABS}. In Fig. 3(a), we have used a high Zeeman splitting of $E_{ZL,R} = 1.5\,\Delta$, resulting in a

sweet spot with relatively high MP, whereas we have used $E_{ZL,R} = 0.15\,\Delta$ in Fig. 3(b), yielding a low-MP sweet spot (for all the parameters used, see the caption of Fig. 2). In both plots, we indicate the location of the even-odd degeneracy with a white line and the location of the sweet spot is marked with a green cross. In both cases, the sweet spot indeed coincides with a maximum of $\mathcal{C}^{(4)}$ along the degeneracy. Figures 3(c) and 3(d) show the same two situations, now as a function of independent ε_L and ε_R, with fixed $\varepsilon^{ABS} = -0.329\,\Delta$ (c) and $\varepsilon^{ABS} = -0.564\,\Delta$ (d). In this case, the correlation between the maximum $\mathcal{C}^{(4)}$ and MP is even more clear than in Figs. 3(a) and 3(b).

This indeed suggests that local tunneling spectroscopy combined with quantum capacitance measurements could provide enough information to identify the sweet spots in parameter space. The method only relies on finding the maximum of $\mathcal{C}^{(4)}$ within the even-odd ground-state degeneracy manifold. This tuning method provides more information than transport measurements alone—which can only determine conditions for ground-state degeneracies—as it is insensitive to details such as QD level arms and cross capacitances between different gates. However, quantum capacitance measurements cannot distinguish between high- and low-MP sweet spots. To distinguish them, experiments probing the non-Abelian properties of the PMMs are required and are discussed in Sec. VII.

V. INITIALIZATION AND READOUT

To go beyond transport spectroscopy and approach Majorana qubits and eventually non-Abelian physics, the first step is to develop the ability to initialize and read out the state associated with a pair of PMMs. Here, the lack of topological protection of the PMMs turns into an advantage. The ground state is singly degenerate everywhere, except for fine-tuned situations that include the sweet spot, where well-separated PMMs appear. Thus, to initialize the system we can simply shift the orbitals of both QDs away from the sweet spot (the degeneracy is not lifted for small shifts of the orbital of only a single QD, although the PMM localization is affected [46]).

Figures 4(a) and 4(b) show the energy differences δE_n between the lowest excited states $n = 1, 2, 3$ and the ground state as a function of the detuning from the sweet spot (solid and dotted blue lines; left vertical axes), for a sweet spot with high MP in Fig. 4(a) and low MP in Fig. 4(b) (using the same parameters as in Fig. 2). Here, we have chosen a symmetric detuning, $\delta\varepsilon_L = \delta\varepsilon_R$, where $\delta\varepsilon_j$ is the deviation of ε_j from the sweet-spot value. For symmetric detuning, the ground state is even, while an asymmetric detuning ($\delta\varepsilon_L = -\delta\varepsilon_R$) would give an odd ground state. Initialization is most easily done by detuning to a point where the even-odd splitting is larger than the thermal energy and waiting for a time longer than the quasiparticle poisoning time.
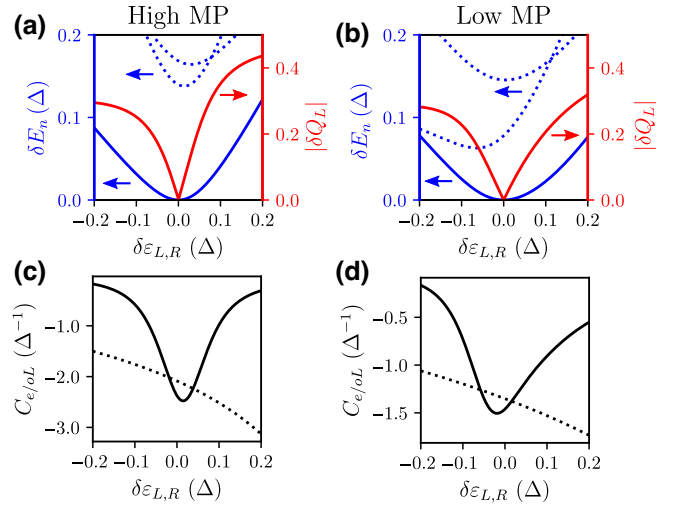

FIG. 4.   (a),(b) The excitation energies δE_n (solid and dotted blue lines; left vertical axes) and absolute value of the charge difference $|\delta Q_L|$ between even and odd ground states on the left QD (red lines; right vertical axes) as a function of detuning both QD orbitals symmetrically ($\varepsilon_L = \varepsilon_R$) away from the sweet spot. (c),(d) Similar to (a),(b) but showing instead the quantum capacitance associated with the left QD of the even ground state (C_{eL}, solid) and odd ground state (C_{oL}, dotted). Parts (a) and (c) correspond to parameters where the MP is high at the sweet spot, while (b) and (d) correspond to parameters where the MP is low at the sweet spot [the same parameters as in Figs. 2(c) and 2(d)].

The conceptually simplest way to read out the state encoded in the two MBSs is through charge detection on one (or both) QDs, similar to what is done for spin qubits [88–92]. This does not give a signal at the sweet spot, where the charge on both QDs is equal in the even and odd states. However, as the QD orbitals are detuned, a substantial charge difference develops; see the red lines (right vertical axes) in Figs. 4(a) and 4(b), which show $|\delta Q_L| = |\langle e|Q_L|e\rangle - \langle o|Q_L|o\rangle|$. This parity-to-charge conversion is similar to the spin-to-charge conversion used for single-shot readout of spin qubits in double QDs [90].

Another option is to read out the state based on a measurement of the quantum capacitance introduced in Sec. IV C (see, e.g., Refs. [93–95]). For readout, we want to measure the quantum capacitance of an individual QD, which is plotted in Figs. 4(c) and 4(d) for a high- and low-MP sweet spot, respectively. At the sweet spot, $C_{ej} \approx C_{oj}$, the difference approaches zero as the MP approaches unity and is exactly zero at the sweet spot in the spinless model in Eq. (5). However, away from the sweet spot, the quantum capacitances differ substantially between the lowest even and odd states. Just as for charge detection, we can therefore use a quantum capacitance measurement for readout if we first detune the system away from the sweet spot.

We note that it is also possible to construct a setup that allows reading out the state while keeping the system at

the sweet spot [46,103]. However, adding detectors capable of readout at the sweet spot not only complicates the device and measurements (requiring either measurements sensitive to charge fluctuations or capacitive coupling to both QDs) but also necessarily introduces a decoherence mechanism at the sweet spot (which will be relevant when we consider coupled PMM systems below). We, therefore, believe that it is better to use simpler readout schemes, such as those discussed above, which are only sensitive to the state encoded in the PMMs away from the sweet spot.

Using the methods for initialization and readout discussed above, we propose that an important first experiment is to measure the lifetime of the parity of a single PMM system. This will limit the lifetime of a PMM qubit and will be a limiting factor for any experiment probing the non-Abelian nature of the low-energy states. Away from the sweet spot, continuous charge-detection or quantum capacitance measurements should exhibit jumps in the readout signal when quasiparticle poisoning switches the system between even and odd parity, thus revealing the rate for such processes. This requires staying close enough to the sweet spot that the even and odd ground states are not separated by much more than the thermal energy. The magnitude of the jumps in the signal should be reduced when approaching the sweet spot. To measure the parity lifetime at the sweet spot, one could instead initialize the system away from the sweet spot and then tune back to the sweet spot for some waiting time, followed by readout away from the sweet spot.

Finally, we note that the physics discussed in this section is to a large extent independent of the MP at the sweet spot. Both readout methods discussed above (charge-detection and quantum capacitance measurements) work almost equally well for a high-MP sweet spot [Figs. 4(a) and 4(c)] as for a low-MP sweet spot [Figs. 4(b) and 4(d)]. There is no qualitative difference in the spectra between high- and low-MP sweet spots [compare Figs. 4(a) and 4(b)], although the gap to excited states tends to be lower for lower MP. There is also no reason to expect drastic differences in the quasiparticle-poisoning times between PMM systems with high- and low-MP sweet spots. The difference between high and low MP will, however, be clear when coupling two PMM systems, as will be discussed in Sec. VI, and will be of crucial importance for the braiding protocols investigated in Sec. VII.

VI. COHERENT MAJORANA OPERATIONS

In the previous sections, we have described ways to characterize a PMM system, where information is encoded in the parity degree of freedom. However, it is usually not possible to create superpositions of the even- and odd-parity states encoded in a single pair of PMMs (or topological MBSs). Therefore, a Majorana qubit should be
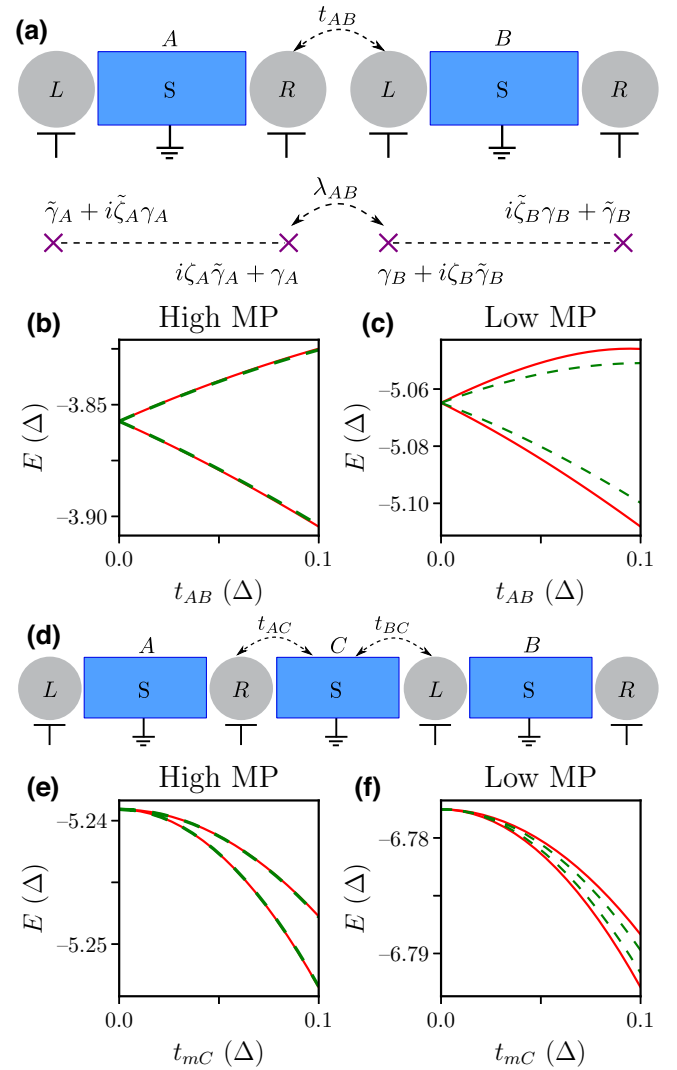

FIG. 5. (a) A sketch of two coupled PMM systems that can be used as a PMM qubit, with the two inner QDs coupled via direct tunneling (upper panel), and a sketch of a low-energy (MBSs-only) model (lower panel). (b),(c) The four lowest eigenenergies of the system in (a) plotted as a function of the QD coupling t_{AB} at (b) a high-MP sweet spot and (c) a low-MP sweet spot (the parameters are the same as for the high- and low-MP sweet spots in Fig. 2 and $t_{AB} = 5t_{AB}^{SO}$). The full red (green dashed) lines show states with total even (odd) parity. (d) The same as (a) but with the inner QDs coupling via a superconducting segment hosting an ABS (and using $t_{AC} = 5t_{AC}^{SO}$). (e),(f) The same as (b),(c) but for the coupling mechanism in (d) ($m = A, B$).

encoded in four PMMs, which can be hosted in two PMM systems with a fixed total parity [3,96].

A. Coupled double quantum dots

We consider two different realizations of the coupling between two PMM systems, as shown in Figs. 5(a) and 5(d). We denote the two PMM systems by A and B, each of which is described by a Hamiltonian as in Eqs. (1)–(3).

The first way to couple the two PMM systems is by direct coupling between the two closest QDs, described by

$$H_{AB} = \sum_\sigma \left[t_{AB} d^\dagger_{AR\sigma} d_{BL\sigma} + t^{SO}_{AB} s_\sigma d^\dagger_{AR\sigma} d_{BL\bar\sigma} + \text{h.c.} \right]$$
$$+ U_{AB} n_{AR} n_{BL}, \tag{23}$$

where t_{AB} (t^{SO}_{AB}) is the amplitude for spin-conserving (spin-orbit–induced spin-flip) tunneling between the right QD in system A and the left QD in system B and U_{AB} is the inter-QD Coulomb charging energy between those QDs with $n_{AR} = \sum_\sigma n_{AR\sigma}$, $n_{BL} = \sum_\sigma n_{BL\sigma}$. A finite U_{AB} will induce correlations between the charge on the innermost QDs and prevent reaching a sweet spot in any of the individual PMM systems even with the tunnel coupling switched off, and in the following we will assume that $U_{AB} = 0$. Because, in contrast to the individual PMM systems, there is no natural screening by a superconducting coupler, achieving $U_{AB} = 0$ will require some design effort, just as for the extra QD in Sec. IV B.

The complication with an inter-QD charging energy can be circumvented by coupling the two PMM systems via an additional superconducting segment. An additional potential advantage with this coupling is that the whole system can be turned into a four-site Kitaev chain. We describe this superconductor with a Hamiltonian analogous to Eq. (2), while the couplings are described by a Hamiltonian analogous to Eq. (3):

$$H_{ACB} = \sum_\sigma s_\sigma \left[t^{SO}_{AC} d^\dagger_{AR\sigma} c_{C\bar\sigma} + t^{SO}_{BC} c^\dagger_{C\sigma} d_{BL\bar\sigma} \right]$$
$$+ \sum_\sigma \left[t_{AC} d^\dagger_{AR\sigma} c_{C\sigma} + t_{BC} c^\dagger_{C\sigma} d_{BL\sigma} \right] + \text{h.c.}, \tag{24}$$

where t_{mC} (t^{SO}_{mC}) is the amplitude for spin-conserving (spin-flip) tunneling between PMM system $m = A, B$ and the connecting superconductor (C) that has electron annihilation operator $c_{C\sigma}$.

With both ways to couple the two PMM systems, the phase differences between the superconductors become important, which can be transformed into phases in the couplings t_{AB} or t_{AC}, t_{BC}. In the results presented in Fig. 5, we have taken all such couplings to be real, which in general will require connecting the different superconductors in a loop to allow phase control. This control is not crucial for the physics discussed here but, as we will see below, it is advantageous for suppressing undesired PMM couplings for low-MP sweet spots.

We consider a setup where the couplings between PMM systems A and B (via either of the two mechanisms described above) can be controlled via gate voltages. If PMM systems A and B are both tuned to a sweet spot and the coupling between them is switched off, the ground state is fourfold degenerate. We can choose to operate the system within the subspace with total even or odd parity, spanned by $|ee\rangle = |e\rangle_A |e\rangle_B, |oo\rangle$ and $|eo\rangle, |oe\rangle$, respectively. Transitions between the total-even- and total-odd-parity subspaces can only happen via quasiparticle poisoning.

When the coupling between the PMM systems is switched on, the fourfold-degenerate ground state splits as seen in Figs. 5(b) and 5(c) for the direct coupling [Eq. (23)] and in Figs. 5(e) and 5(f) for the coupling via an additional superconducting segment [Eq. (24)]. For small coupling strength (compared with the couplings within each PMM system), the main difference between the two coupling mechanisms is that for coupling via an additional superconducting segment, the effective coupling between QDs AR and BL is of second order in the couplings t_{mC} and t^{SO}_{mC} to the ABS (although the details will depend on the energy of the ABS). We furthermore compare the cases of high and low MP. Figures 5(b) and 5(e) show that for a system tuned to a high-MP sweet spot, switching on the coupling splits the fourfold-degenerate ground state into two (nearly) twofold-degenerate states. This corresponds to an equal splitting within the even- (red full lines) and odd- (green dashed lines) parity subspaces. In contrast, lower MP leads to a different splitting within the total-even- and total-odd-parity subspaces and thus to a complete breaking of the ground-state degeneracy [see Figs. 5(c) and 5(f)].

We can understand the MP dependence of the spectra by comparing with the low-energy model introduced in Eq. (8) generalized to two coupled PMM systems,

$$H^{\text{lowE}}_{AB} = \frac{i}{2} \sum_{s=A,B} \xi_s \gamma_s \tilde\gamma_s$$
$$+ \frac{i}{4} \left[\lambda_{AB}(\gamma_A - i\zeta_A \tilde\gamma_A)(\gamma_B + i\zeta_B \tilde\gamma_B) - \text{h.c.} \right], \tag{25}$$

where we have chosen the Majorana operators such that the ground states on the inner QDs (AR and BL) are dominated by γ_s but also contain an additional small fraction ζ_s of $\tilde\gamma_s$ (see Sec. II C). This model is illustrated in the lower panel of Fig. 5(a). Formally, we can obtain the coupling term from the spinless model by projecting the electron operators $d^{(\dagger)}_{AR}$ and $d^{(\dagger)}_{BL}$ onto the low-energy fermion in Eq. (7) and then reexpressing the result in terms of the Majorana operators in Eq. (8). The coupling λ_{AB} can also induce terms $\propto \gamma_s \tilde\gamma_s$ but they will scale as λ^2_{AB} and we will neglect them in the following, where we focus on small λ_{AB}. The connection between ζ and the MP is given by Eq. (16), although this expression should not be used for a very small Zeeman energy (leading to small MP), where the low-energy model is not appropriate.

As mentioned above, the coupling between the PMMs depends on the phase of λ_{AB}, which can be controlled if the superconductors are connected in a loop. Just as in Fig. 5,

we focus below on real $\lambda_{AB} > 0$, where Eq. (25) simplifies to

$$H_{AB}^{\text{lowE}} = \frac{i}{2} \sum_{s=A,B} \xi_s \gamma_s \tilde{\gamma}_s$$
$$+ \frac{i\lambda_{AB}}{2}(\gamma_A \gamma_B + \zeta_A \zeta_B \tilde{\gamma}_A \tilde{\gamma}_B). \quad (26)$$

If each PMM system is at a sweet spot when the coupling is switched off, then $\xi_s = 0$ by definition. If, in addition, we have perfect PMMs at the sweet spot, the MP is unity and $\zeta_s = 0$, and Eq. (26) shows that turning on λ_{AB} leads to an equal splitting within the subspaces with total even and total odd parity [see Figs. 5(b) and 5(e)]. This splitting corresponds to a finite energy of the fermion $f_\alpha = (\gamma_A + i\gamma_B)/2$ but a preserved twofold degeneracy associated with the uncoupled fermion $f_\beta = (\tilde{\gamma}_A - i\tilde{\gamma}_B)/2$ (for an explanation for the specific forms of f_α and f_β, see Appendix A). For imperfect PMMs—MP less than unity and $|\zeta_s| > 0$—also, $\tilde{\gamma}_A$ and $\tilde{\gamma}_B$ couple, leading to a finite energy of the fermion f_β and thus to a breaking of the remaining twofold degeneracy. As a consequence, the splittings within the subspaces with even and odd total parity are no longer equal. This is what is seen in Figs. 5(c) and 5(f) as a splitting between the full red and dashed green lines [note that for an even ground state, one must take $\zeta_A = -\zeta_B$ in Eq. (26)].

We note here that there is, in fact, an important advantage in using phase control to achieve a real λ_{AB}. Compared with Eq. (25), the terms that are linear in ζ_s have vanished in Eq. (26). Thus, a real λ_{AB} reduces the effect of imperfect PMMs (low MP).

It is exactly this additional splitting for finite ζ_s that will be the deciding factor for whether or not the braiding protocols in Sec. VII work. It is therefore desirable to accurately measure the breaking of the ground-state degeneracy in two coupled PMM systems. One way would be to simply measure the spectrum for a finite coupling with transport spectroscopy (similar to Sec. IV A). However, we will now show that by operating the coupled PMM systems as a qubit in both the total-even-parity and total-odd-parity subspaces, the breaking of the ground-state degeneracy can instead be measured in the time domain, which should allow for the detection of much smaller energy splittings.

B. Coherent control of Majorana qubits

We start by considering a qubit encoded in the subspace with even total parity, such that $|ee\rangle$ is at the north pole and $|oo\rangle$ is at the south pole of the Bloch sphere. Then, detuning one or both PMM systems away from the sweet spot with the coupling between them switched off causes a rotation around the z axis, while coupling the two PMM systems results in a rotation around an axis in the x-y plane. This becomes clear if we approximate the coupled PMM

systems by the low-energy four-MBS Hamiltonian given in Eq. (26). If we choose

$$\gamma_s = f_s^\dagger + f_s, \quad \tilde{\gamma}_s = i(f_s^\dagger - f_s), \quad (27)$$

with $f_s^\dagger$ being the creation operator for a fermion in the lowest-energy mode in PMM system $s = A, B$, then $|ee\rangle$ is the ground state of the uncoupled system for $\xi_s > 0$ and we identify the Pauli matrices as $\sigma_z = -i\gamma_A \tilde{\gamma}_A = -i\gamma_B \tilde{\gamma}_B$, $\sigma_y = i\gamma_A \gamma_B = -i\tilde{\gamma}_A \tilde{\gamma}_B$, and $\sigma_x = -i\gamma_A \tilde{\gamma}_B = -i\tilde{\gamma}_A \gamma_B$ (where the equality signs should be interpreted as the operators having the same effect within the total-even-parity subspace). Thus, within the total-even-parity subspace Eq. (26) becomes

$$H_{AB,e}^{\text{lowE}} = -\frac{\xi_+}{2}\sigma_z + \frac{\lambda_{AB}}{2}(1 - \zeta_A \zeta_B)\sigma_y, \quad (28)$$

where $\xi_+ = \xi_A + \xi_B$.

We now discuss how to initialize, control, and read out the PMM qubit. For simplicity, we base our discussion on the low-energy model in Eq. (28) but the same operations also work when this is not a good approximation. The qubit can be initialized in an eigenstate of σ_z by letting $\lambda_{AB} \to 0$ and detuning the QDs away from the sweet spot to make $\xi_A \neq 0$ and $\xi_B \neq 0$. This can be followed by either a parity measurement as described in Sec. V or simply by letting the system relax (by quasiparticle poisoning) to the ground state, before tuning back to the sweet spot. Two-axis control of the qubit is achieved by pulsing ξ_s (resulting in a rotation around the z axis) or λ_{AB} (resulting in a rotation around the y axis). Readout is performed in the same way as initialization with λ_{AB} switched off.

Even if one has braiding as the end goal, qubit measurement is an important stepping stone. In addition to being a test of initialization, coupling, and readout, it allows measurements of the coherence time (T_2 time), which will also be a limiting factor for braiding. This can be done simply by measuring the decay of coherent oscillations with a finite λ_{AB} or in a Ramsey-type experiment where one first performs a $\pi/2$ rotation into the x-y plane, then waits for some time before applying another $\pi/2$ rotation, giving a decaying signal as a function of the waiting time. Furthermore, the frequency of coherent oscillations provides a measure of ξ_+, allowing for tuning to even-odd degeneracy without being limited by thermal broadening. This experiment in itself is not sensitive to ζ and we can equally well implement a qubit based on PMMs with low MP, although there is a slight lifting of the protection from variations in QD orbital energies that will likely affect the coherence times at very low MP.

For the purpose of estimating ζ (or the MP), we now consider a qubit encoded instead in the subspace of total odd parity, where we choose $\sigma_z = -i\gamma_A \tilde{\gamma}_A = i\gamma_B \tilde{\gamma}_B$, $\sigma_y = i\gamma_A \gamma_B = i\tilde{\gamma}_A \tilde{\gamma}_B$, and $\sigma_x = i\gamma_A \tilde{\gamma}_B = -i\tilde{\gamma}_A \gamma_B$ (where

the equality signs should be interpreted as the operators having the same effect within the total-odd-parity subspace). Then, we obtain

$$H_{AB,o}^{\text{lowE}} = -\frac{\xi_-}{2}\sigma_z + \frac{\lambda_{AB}}{2}(1 + \zeta_A\zeta_B)\sigma_y, \qquad (29)$$

where $\xi_- = \xi_A - \xi_B$.

Comparing the second terms in Eqs. (28) and (29) shows that for the same value of λ_{AB}, the effective coupling strength is different in the even and odd subspaces. This reflects the different splitting between the two green dashed lines compared with the splitting between the two red full lines in Figs. 5(c) and 5(f). Thus, the difference in qubit rotation frequency around the y axis for a given λ_{AB} between the qubit in the even and odd subspaces provides a time-domain measurement of the Majorana quality.

It is important to note that at the sweet spot and with the coupling between the PMM systems switched off, the total-even- and total-odd-parity ground states are degenerate. Thus, the total-even- and total-odd-parity qubits will be operated with all parameters identical and the only difference during operation will be in the initialization. To initialize in the total odd subspace, we detune one PMM system away from the sweet spot to give an even-parity ground state (which can, e.g., be done by setting $\varepsilon_{AL} = \varepsilon_{AR}$) but the other one to give an odd-parity ground state (which can, e.g., be done by setting $\varepsilon_{BL} = -\varepsilon_{BR}$).

C. Testing Majorana fusion rules

A Majorana fusion experiment has been suggested as a probe of non-Abelian physics that is experimentally easier than braiding [81,82,98–103]. Here, we briefly discuss and comment on a fusion protocol for PMMs that is similar in spirit to that in Ref. [81] and analogous to the recent proposal in Ref. [103]. The aim of a fusion protocol is to initialize Majorana pairs and thereafter measure them in a different pairing configuration. The possible outcomes of this measurement (fusion) and the associated probabilities are a fundamental property of non-Abelian anyons. The simplest version of the fusion protocol requires four PMMs and can be accomplished in either of the setups sketched in Figs. 5(a) and 5(d) [where $U_{AB} \approx 0$ is needed for the setup in Fig. 5(a)] through the following steps:

(i) The protocol starts with a large coupling between the two PMM systems. If the MP is high, the ground state is almost twofold degenerate [Figs. 5(b) and 5(e)] but we can break that degeneracy by detuning the outermost QDs, AL and BR. The system is then allowed to relax to the unique ground state before bringing the levels of QDs AL and BR back to their sweet-spot values. With true topological MBSs, which is described by the low-energy model in Eq. (25) with $\zeta_A = \zeta_B = 0$, this corresponds to

initializing the system in a state where the innermost (γ_A and γ_B) and outermost ($\tilde{\gamma}_A$ and $\tilde{\gamma}_B$) PMM pairs have a definite parity. A PMM system with $|M_{AR}| < 1$ and/or $|M_{BL}| < 1$ can be approximated by $|\zeta_A| > 0$ and/or $|\zeta_B| > 0$, in which case all four PMMs couple and the initial state deviates from the ideal one.

(ii) In the next step, we reduce the coupling between the two PMM systems. This should be done adiabatically with respect to higher-energy states [not shown in Fig. 5 but corresponding to excitations within each PMM system of the type in Figs. 4(a) and 4(b)]. At the end of this step, the ground state is (almost) twofold degenerate independent of the MP, with a possible splitting set by a combination of residual coupling (if this cannot be switched off completely) and a finite energy of each individual PMM system if it has not been tuned perfectly to the sweet spot [corresponding to finite ξ_s in Eqs. (25) and (26)]. The operation of switching off the coupling should be fast compared to the inverse of that energy scale.

(iii) Finally, the state of the PMM pairs within each PMM system is read out. The readout can be done as described in Sec. V by detuning away from the sweet spot with the coupling between PMM systems switched off. In the ideal case, this corresponds to reading out the eigenvalue of $i\gamma_s\tilde{\gamma}_s$ in Eqs. (25) and (26).

Thus, in the ideal case, the fusion protocol will initialize the system in an eigenstate of $i\gamma_A\gamma_B$ and $i\tilde{\gamma}_A\tilde{\gamma}_B$ and then read out this state in the eigenbasis of $i\gamma_A\tilde{\gamma}_A$ and $i\gamma_B\tilde{\gamma}_B$. According to the Majorana fusion rules, the outcome of the readout is 50-50 (because of conservation of total parity, there are two possible outcomes).

In principle, there is no problem associated with implementing this protocol in the setup with imperfect PMMs. The problem is, instead, that the protocol will also work for low-MP PMMs. In fact, as was noted in Ref. [98], the outcome of a fusion protocol as sketched above (or any of the versions that are based on the same principle) will always be 50-50, as long as the protocol is diabatic with respect to the small ground-state splitting mentioned in step (ii) above but adiabatic with respect to all higher excited states. We show this in detail in Appendix A, where we demonstrate that the low-energy model in Eq. (26) produces a 50-50 outcome independent of the values of ζ_s, i.e., independent of the MP values. Thus, the protocol serves as a time-domain probe of the exactness of the ground-state degeneracy and is a useful test of adiabatic control of the PMM system but it does not give conclusive evidence of the actual Majorana nature of the associated (near) zero-energy fermionic states. Therefore, we now turn to braiding experiments.

VII. NON-ABELIAN SIGNATURES AND MAJORANA BRAIDING

Exchanging two MBSs leads to a nontrivial change in the system state, which serves as direct evidence of their non-Abelian properties. However, physically exchanging MBSs is challenging and hence various protocols have been proposed that have the same effect on the states encoded by the MBSs but that are hopefully easier to realize experimentally. In this section, we adapt three such proposals for the PMM platform and investigate the impact of the unavoidable imperfect nature of the PMMs. Throughout this section, we describe the PMM systems with appropriately extended versions of the low-energy model in Eqs. (25) and (26), which implicitly means that we assume that inter-QD Coulomb interactions are negligible or can be compensated for by gating.

A. Non-Abelian signatures in charge-transfer-based protocols

Charge-transfer-based protocols [83,106,107] provide conceptually simple tests of Majorana non-Abelian properties. The basic setup (adapted to our PMM systems) is sketched in Fig. 6(a) and the protocol is based on transferring charges between the central QD (D) and the PMM systems by sweeping the level of QD D from negative to positive (or from positive to negative) energies. In an adiabatic operation, a single charge is transferred between QD D and the coupled PMMs, thereby changing the joint fermion parity of the two PMM systems. When QD D couples to a single PMM (e.g., γ_A), the operation can be understood mathematically as acting with the corresponding Majorana operator, $C_i = \gamma_A$ on the ground state of the PMM system. If QD D is coupled to a pair of PMMs (say, γ_A and γ_B), the charge-transfer operation can be understood as acting with the operator $F_{AB} = (\gamma_A + \gamma_B)/\sqrt{2}$ on the PMM systems. Therefore, $B_{AB} = F_{AB}C_A$ gives the same result as braiding PMMs γ_A and γ_B and the difference between $C_A F_{AB}$ and $F_{AB}C_A$ is due to the non-Abelian nature of the PMMs. It might be more convenient to add a third operation, i.e., $F_{AB}C_A F_{AB}$ and $F_{AB}F_{AB}C_A$, so that, for perfect PMMs, each sequence gives a state with well-defined PMM parities, differing only by the fermion between the left and right subsystems [107].

To see how this protocol is affected by having PMMs with MP less than unity, we generalize the low-energy model in Eq. (25) to include the extra QD D in Fig. 6(a):

$$H = \omega_D d_D^\dagger d_D + \frac{i}{2}\sum_{s=A,B} \xi_s \gamma_s \tilde{\gamma}_s$$

$$+ \frac{i}{2}\sum_{s=A,B}[\lambda_s(\gamma_s - i\zeta_s\tilde{\gamma}_s)d_D - \text{h.c.}]. \quad (30)$$
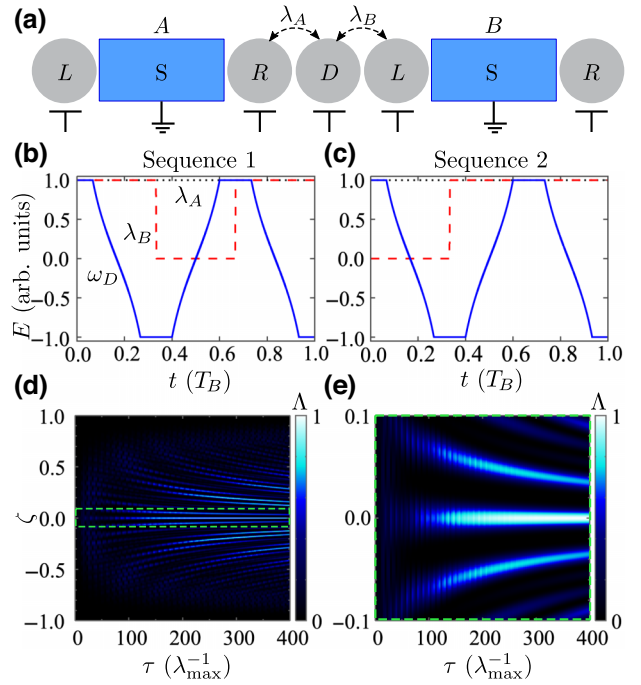

FIG. 6. The charge-transfer protocol for demonstration of PMM non-Abelian properties. (a) A sketch of the setup with QD D tunnel coupled to the two PMM systems. (b),(c) The two sequences of the protocol, where the energy of QD D is swept between positive and negative energies (T_B is the duration of each sequence). To minimize the effect of dynamical phases, we sweep QD D as $\omega_D(t) = \omega_D^{\max}\tan[\pi/4(t-t_0)/\tau]$, where t_0 is a time offset and τ controls the sweep time. The energies are normalized with respect to their maximum values, taken as $\lambda_A^{\max} = \lambda_B^{\max} = \omega_D^{\max}/500 = \lambda_{\max}$ (used as the energy unit in the figure). (d) The protocol visibility Λ, defined as the product of the probabilities of finding the ideal Majorana outcome after sequences 1 and 2. For the initial state $|ee\rangle$, $\Lambda = P_{oe}^1 P_{eo}^2$. (e) Close-up of the plot in (d) close to $\zeta = 0$.

The system is first initialized by detuning the PMM QDs, as explained in Sec. V. Sweeps of QD D can flip the parity of the A and B PMM systems. To implement F_{AB}, we keep the tunnel rates to A and B equal ($\lambda_A = \lambda_B$), while C_A can be achieved by setting $\lambda_B = 0$. The two different sequences are sketched in Figs. 6(b) and 6(c).

We test the protocol numerically by solving the time-dependent Schrödinger equation for the unitary time evolution while sweeping the level of QD D up and down according to Figs. 6(b) and 6(c). For these sweeps, we use a shape that minimizes the accumulation of dynamical phases [107]. For a system initialized in the state $|ee\rangle = |e\rangle_A|e\rangle_B$, the ideal outcome for sequence 1 (2) is $|oe\rangle$ ($|eo\rangle$), which can be measured using the parity readout described in Sec. V. Deviations from these outcomes are associated with imperfectness of the charge-transfer operations (as discussed in Refs. [106,107]) and/or the less-than-unity MP (finite ζ_s). Figure 6(d) shows the protocol visibility,

Λ, given by the product of the probabilities that the two sequences give the result expected for perfect Majoranas.

The numerical calculations show small regions where $\Lambda \approx 1$, including the PMM sweet spot, $\zeta = 0$. The failure of the protocol for larger ζ is due to the finite splitting of the degenerate manifold, which depends linearly on ζ. This splitting introduces a dynamical phase and, therefore, a dependence of the final state on the details of how operations are performed. Therefore, a minimization of the dynamical phase would require fast operations, although slow enough to avoid nonadiabatic effects (which lead to failure of the protocol for too fast sweeps, even for $\zeta = 0$). This trade-off results in a relatively narrow range close to $\zeta = 0$, where the designed sequences of operations can show Majorana non-Abelian properties. In principle, it might be possible to extend the ζ range where the protocol is successful by echoing away the dynamical phase, e.g., by reversing the sign of ζ between operations (similar to the echo used to compensate for an imperfectly fine-tuned phase in Ref. [107]).

B. Measurement-based braiding

Another way of effectively performing braiding and operations on a set of MBSs is by using a measurement-based protocol [84,85,108]. A protocol that uses QDs to read out the parity of pairs of MBSs and performs a braiding has been presented in Ref. [85]. Here, we discuss how this protocol can be adapted to PMMs. The setup shown in Fig. 7(a) contains three PMM systems (A, B, and C) and two additional QDs for parity readout (U and D). PMM system s hosts two PMMs, γ_s, localized mainly on QD sL, which is connected to one or two readout QDs, and $\tilde{\gamma}_s$, which is localized mainly on QD sR and is not connected to any readout QD. PMM systems A and B together have a doubly degenerate ground state for a given parity, which can be manipulated by braiding. PMM system C provides a pair of auxiliary PMMs.

Let us start by describing the procedure for the case where all PMMs have unit MP. The aim will be to braid γ_A and γ_B. This can be done through the following sequence of measurements: (i) initialize the joint parity of γ_C and $\tilde{\gamma}_C$ to be even; (ii) measure the joint parity of γ_A and γ_C; (iii) measure the joint parity of γ_B and γ_C; and (iv) measure the joint parity of the auxiliary PMMs γ_C and $\tilde{\gamma}_C$, which we postselect for an even outcome. After this sequence, one has performed an operation identical to a braiding of γ_A and γ_B if the outcomes of measurements (ii) and (iii) are both even (see Ref. [85]) [for different outcomes of (ii) and/or (iii), the result deviates from the ideal braiding by a phase]. More formally, the operator B_{AB} for braiding γ_A and γ_B can be realized by the following set of projections:

$$B_{AB} \propto M_{C\tilde{C}} M_{BC} M_{AC} M_{C\tilde{C}}, \quad (31)$$
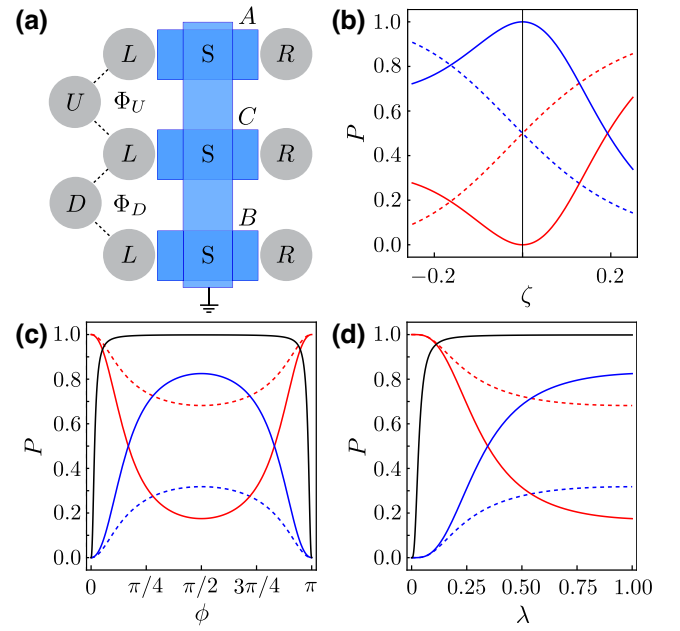

FIG. 7. Measurement-based braiding. (a) A sketch of the proposed device, consisting of three PMM systems (A, B, and C) and two readout QDs (U and D). (b)–(d) The outcomes of the braiding protocols for single (dashed line) and double (solid lines) braids, starting from the state $|eee\rangle = |e\rangle_A |e\rangle_C |e\rangle_B$. The lines represent the weights (P) of the final states. The red curves give the probability for staying in the initial state, $|eee\rangle$, while the blue curves give the probability for ending up in the other even state, $|oeo\rangle$. (b) The braiding outcome as a function of $\zeta = \zeta_A = \zeta_B = \zeta_C$ with $\lambda = 1$ and $\phi = \pi/2$. (c) The braiding outcome as a function of ϕ for $\lambda = 1$ and $\zeta = 0.1$. (d) The braiding outcome as a function of λ with $\phi = \pi/2$ and $\zeta = 0.1$. The full black lines show for comparison the probability of the double braid to end up in the $|oeo\rangle$ state with very high-quality PMMs ($\zeta = 0.01$). For this close-to-ideal case, the results are nearly independent of λ and ϕ.

where $M_{ss'}$ ($M_{s\tilde{s}}$) denotes a projective measurement onto the state with even parity of γ_s and $\gamma_{s'}$ (γ_s and $\tilde{\gamma}_s$).

The projection $M_{C\tilde{C}} = (1 + i\gamma_C\tilde{\gamma}_C)/2$ is done as described in Sec. V and can, in principle, be perfect independent of the MP. We now discuss readout of the joint parity of γ_A and γ_C using readout QD U, which is done along the lines described in Refs. [83–87]. The readout of the parity of γ_B and γ_C is completely analogous. For MP less than unity, these readouts will not be perfect, which will lead to deviations from the ideal braiding result.

The readout QD U is coupled to QD AL (CL) with tunnel amplitude λ_{AU} (λ_{CU}) and the coupled system can be described by a Hamiltonian completely analogous to Eq. (30). First, we note that the coupling of the PMM systems to a single-level QD can only decrease the degeneracy by 2. This is because a single fermion coupled to a

degenerate subspace consisting of N fermions will necessarily yield $N - 1$ dark fermions [126]. The readout QD U thus splits the system according to the occupation of the fermionic mode to which it couples and after some rather lengthy algebra (see Appendix B), one can express the parity operator that couples to QD U in terms of the parameters ζ_s, $\phi = \arg(\lambda_{AU}/\lambda_{CU})$, and $\lambda = |\lambda_{AU}/\lambda_{CU}|$. When the coupling is switched on, it will constitute a measurement of this parity operator. If the coupling is not too strong, the system ends up in one of its two energy eigenstates [86,87,127,128]. The maximal visibility turns out to be achieved for $\phi = \pi/2$ and $\lambda = 1$.

This projection varies between the ideal topological case discussed above for all $\zeta_s = 0$ to the "trivial" (or fermionic) case for $\zeta_s = 1$. However, the fermionic case is actually not as trivial as one might expect. For $\zeta_s = 1$ and the initial state $|oee\rangle = |o\rangle_A |e\rangle_C |e\rangle_B$, the braiding protocol of Eq. (31) gives $B_{AB}|oee\rangle = |eeo\rangle$, perhaps as expected. However, a double braid (i.e., acting twice with B_{AB}) annihilates the state. The braiding protocol also annihilates $|eee\rangle$ and $|eeo\rangle$, whereas $|oeo\rangle$ is an eigenstate of B_{AB}. To conclude, the braiding operation does not necessarily give the "trivial" braiding of electrons in the fermionic limit.

The protocol gives the outcome expected for topological MBSs only for all $\zeta_s = 0$. In the small-ζ regime, there are some deviations from the ideal braiding results. This is shown in Fig. 7(b), where the outcomes of single and double braids are shown as a function of $\zeta = \zeta_A = \zeta_B = \zeta_C$. Figures 7(c) and 7(d) show the stability of the braiding outcome when changing ϕ and λ. For ideal PMMs, the outcome of the protocol does not depend on these parameters (although the visibility of the readout signal does, such that readout might become difficult far from $\phi = \pi/2$ and $\lambda = 1$).

To conclude this subsection, the presented measurement-based protocol could in principle be used to demonstrate PMM braiding. However, the interpretation might become difficult, because the results will depend strongly on the device parameters, such as magnetic fluxes, gate-voltage settings, and tunnel couplings. On the other hand, this dependence might be a very useful way to characterize the device.

C. Hybridization-induced braiding

The hybridization-induced braiding protocol relies on alternating couplings between MBSs to effectively exchange their positions. There are many versions of this protocol in the literature for braiding of topological MBSs [14,80–82,98,109,110], which differ from each other mainly in the physical mechanism used to realize MBS coupling, initialization, and readout. Our proposed PMM version is based on the setup in Fig. 8(a) with three PMM systems and resembles the setup in Ref. [105] (which, however, focuses on real-space braiding). To describe this system, we use a generalization of Eq. (26),

$$H = \sum_s \frac{i\xi_s}{2} \gamma_s \tilde{\gamma}_s + \frac{i}{2} \sum_{ss'} \lambda_{ss'}(\gamma_s \gamma_{s'} + \zeta_s \zeta_{s'} \tilde{\gamma}_s \tilde{\gamma}_{s'}), \quad (32)$$

where $ss' = AB, BC, AC$ and we have taken the coupling terms $\lambda_{ss'}$ to be real, which requires phase control of the superconductors. As in Sec. VI, ζ_s is a measure of the relative amplitude of the outer-QD PMMs $\tilde{\gamma}_s$ on the inner coupled QDs, such that $\zeta_s = 0$ for unit MP.

The hybridization-induced braiding protocol requires tuning the couplings between three PMMs [14,80–82,98,109,110] and the different steps involved are schematically illustrated in Fig. 8(b). In the first step, all couplings between PMM systems are switched off (all $\lambda_{ss'} = 0$) and the system is initialized in a state with a well-defined fermion parity in subsystems A and B, which are tuned to the Majorana sweet spot ($\xi_A = \xi_B = 0$). The ground-state degeneracy of the central subsystem is split ($\xi_C \neq 0$) by coupling the two PMMs γ_C and $\tilde{\gamma}_C$, which is represented by a green dashed line in Fig. 8(b). The initialization and degeneracy breaking within each PMM system is described in Sec. V.

The aim of the protocol is then to exchange PMMs γ_A and γ_B. During the protocol, λ_{AC}, λ_{BC}, and ξ_C are switched on and off in a specific sequence, as shown in Figs. 8(b) and 8(c). At each step, one or two (but never three or zero) couplings are switched on. For PMMs with unit MP ($\zeta_A = \zeta_B = \zeta_C = 0$), this guarantees that the ground state remains twofold degenerate within a subspace of fixed total parity. The entire protocol is carried out once (single braid) or twice (double braid), after which the parity of subsystem A and/or B is read out (see Sec. V) with all $\lambda_{ss'} = 0$.

For definiteness, we assume that the system is initialized in the state $|ee\rangle = |e\rangle_A |e\rangle_B$ (in the calculation PMM system C is also initialized to be even but this is not important and we suppress it in our notation). The ideal result of exchanging PMMs γ_A and γ_B once (one sequence of the braiding protocol) is to transform the state according to

$$|ee\rangle \rightarrow \frac{1}{\sqrt{2}}(|ee\rangle + i|oo\rangle). \quad (33)$$

Carrying out the same sequence twice brings γ_A and γ_B back to their original positions but the state is transformed according to

$$|ee\rangle \rightarrow |oo\rangle. \quad (34)$$

Readout of the parity of either PMM system A or B is sufficient to detect successful braiding but readout of both provides a consistency check and, also, readout of PMM system C can be used to verify that the total parity has
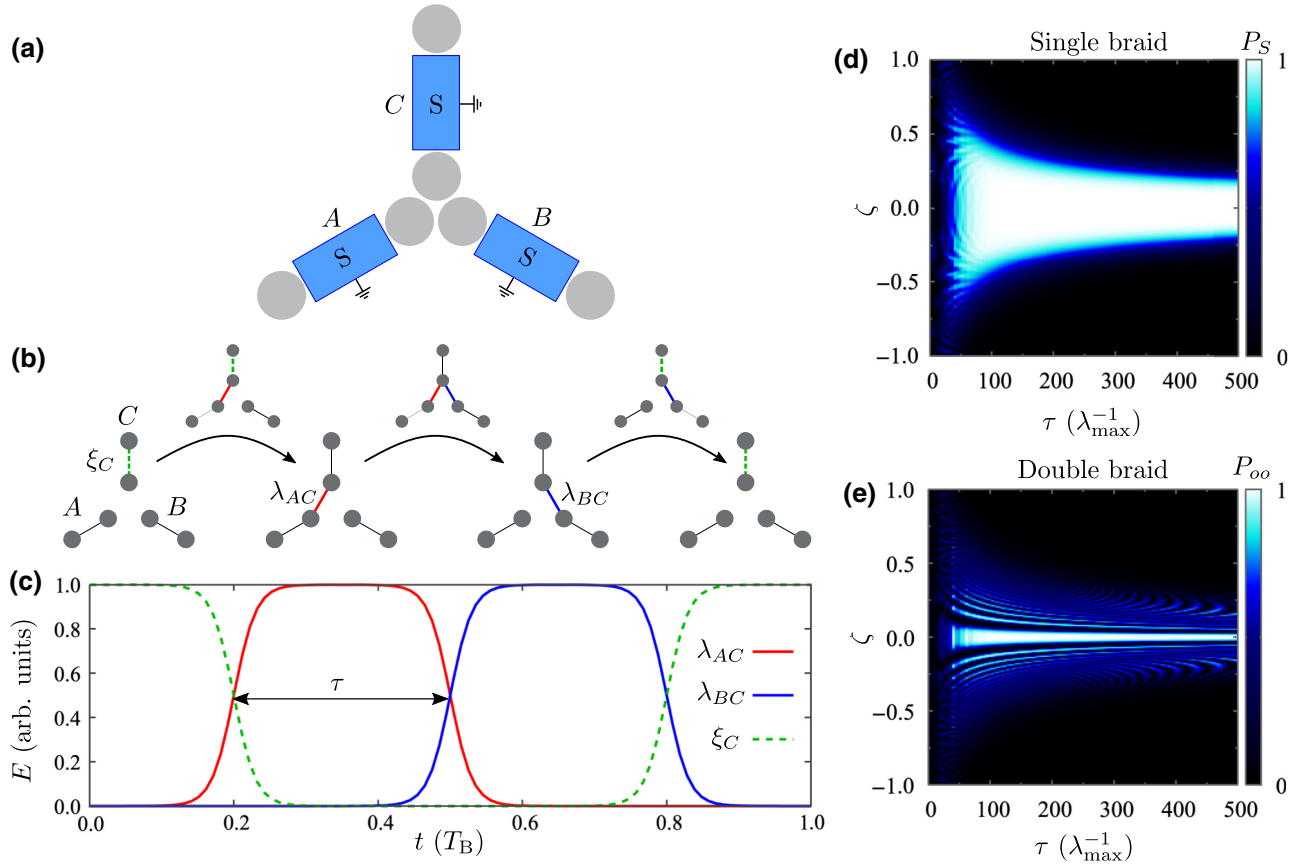
FIG. 8. Hybridization-induced braiding. (a) A sketch of the setup. (b) The braiding protocol, where the coupling between PMM pairs is switched on and off. (c) The strengths of the different couplings during the protocol, as a function of time t normalized by the protocol duration T_B. (d) P_S [as defined in Eq. (35)] after a single braid, as a function of ζ, and the time of each interaction pulse τ (in units of the inverse of λ_max, the maximal value of ξ_C, λ_{AC}, and λ_{BC}). (e) The probability of measuring a parity flip of the PMM systems A and B (= P_{oo} with the chosen initial conditions) after a double braid. We have used $\max(\lambda_{AC}) = \max(\lambda_{BC}) = \max(\xi_C)$, which are switched on and off using a sigmoid function with a rate $r = 50/\tau$.

remained fixed during the protocol (no quasiparticle poisoning). We imagine that the experiment is carried out many times and compare the outcome with the ideal probability distributions from Eqs. (33) and (34). For the single braid, we define the function

$$P_S = 4P_{oo}P_{ee}, \qquad (35)$$

where P_{ee} (P_{oo}) is the probability of measuring even (odd) parity in PMM systems A and B. $P_S = 1$ for the ideal 50-50 outcome and $P_S = 0$ for the trivial outcome of both PMM systems always being even or always being odd. For the double braid, we simply have $P_{oo} = 1$ in the ideal case, while $P_{oo} = 0$ in the trivial case.

We simulate the braiding protocol by solving the time-dependent Schrödinger equation for the model in Eq. (32) with the initial conditions described above. Figure 8(c) shows the calculated result for P_S defined in Eq. (35) after a single braid, as a function of $\zeta = \zeta_A = \zeta_B = \zeta_C$ and τ, the duration of each interaction. Figure 8(c) shows the analogous result for P_{oo} after a double braid.

For $\zeta = 0$, we find the result expected for topological MBSs, $P_S = 1$ and $P_{oo} = 1$ for the single and double braid, respectively. The result for the single braid seems relatively stable for $\zeta \lesssim 0.5$. This is because the quantities that are read out (P_{ee} and P_{oo}) are insensitive to the phase between the $|ee\rangle$ and $|oo\rangle$ components of the wave function in Eq. (33) [98]. However, this phase manifests itself after a second braid operation and the double braid result is therefore much more sensitive to ζ. But also for the double braid, there are special values of the operation speed where a close-to-ideal result is found even for rather large ζ. Thus, we conclude that to prove non-Abelian exchange with PMMs, one should do both single- and double-braid protocols and also vary the speed of the protocol to verify the stability of the result.

VIII. CONCLUSIONS

In this work, we have presented a pathway for next-generation experiments on PMMs in minimal Kitaev

chains. We believe that the ultimate goal of such experiments should be the demonstration of the non-Abelian nature of Majoranas. However, the path contains a few milestones along the way, including assessment of PMM quality (closeness to true topological Majoranas), initialization and readout of the fermion parity encoded in PMMs (including measurements of quasiparticle poisoning times), and coherent control of a PMM qubit and measurements of coherence times.

We have presented three different braidinglike tests of Majorana non-Abelian physics, focusing on how the PMM quality affects the outcome. The suggestion for charge-transfer-based non-Abelian operations is simplest in terms of the required setup, which can be realized in a linear geometry. However, it has the disadvantage of only being partially protected (even for topological Majoranas) and we also show that it only produces a nontrivial result if the PMMs have very high quality. The protocol for measurement-based braiding becomes equivalent to topologically protected braiding for perfect PMM quality but it can also produce non-Abelian (but unprotected) results for low-quality PMMs and care is needed to avoid false-positive outcomes of an experiment. The hybridization-induced braiding most closely resembles the picture of braiding as moving Majoranas around each other, is fully protected for topological Majoranas, and gives a non-trivial outcome for lower-quality PMMs compared with the charge-transfer protocol but requires a comparatively complex geometry and operational protocol.

For all protocols, we emphasize that a true signature of non-Abelian physics must exhibit some kind of stability to be distinguishable from conventional manipulation of a quantum state. For the charge-transfer and hybridization-based protocols, this stability manifests in the result being independent of protocol speed (within some interval). For the measurement-based protocol, the stability is instead with respect to parameters characterizing the coupling between the PMMs and the readout device.

All braiding protocols need to be performed faster than the coherence time and the inverse residual splitting at the sweet spot, both of which can be measured as described in Sec. VI B. Adiabaticity furthermore requires that the operations are slow with respect to the excitation gap. For a high-MP PMM system at the sweet spot, from Fig. 4(a) we find that the excitation gap is approximately 0.15Δ. For an induced superconducting gap in the central (S) part $\Delta = 0.2$ meV, this corresponds to a lower time limit of 20 ps. The operations required for the proposed protocols are fully analogous to those routinely performed in semiconductor spin-qubit platforms based on similar materials [129]. There, operations involving gate-controlled changes of tunnel barriers and QD levels are performed on time scales of nanoseconds and we expect the same to be possible for PMM systems, while the duration of the readout operations is in the order of μs.

With the Majorana delocalization parameter $\zeta = 0.1$ the charge-transfer protocol fails, the measurement-based braiding gives results that deviate by approximately 10–20% from the ideal result and have some stability to variations in phase and tunnel coupling, while the hybridization-induced braiding approaches the ideal stable results even for a double braid (with a single braid also being successful for much larger ζ). Based on Eq. (16), $\zeta = 0.1$ corresponds to an MP value of around 0.98, which seems well within experimental reach (the high-MP case in Figs. 2–5 has an MP value of around 0.986). With $\zeta = 0.01$, all three protocols give a stable and close-to-ideal result. However, this corresponds to an MP value of around 0.9998, which in our spinful model would require $E_Z \approx 20\Delta$ if the rest of the parameters are chosen as in Figs. 2–5 (but significantly higher charging energies would reduce this value [53]). For all protocols, non-Abelian results without significant stability already appear for much larger ζ, which may not be unambiguous evidence for topologically protected non-Abelian physics of Majoranas but is exciting new physics nonetheless.

It would be an interesting direction for future theoretical works to try to optimize the braiding protocols presented here to improve their stability and extend their usefulness to PMM systems with lower MP. This could involve, e.g., optimized pulses and/or echo pulses to minimize or cancel dynamical phases. It would also be interesting to theoretically investigate decoherence in PMM systems and its effect on different braiding protocols. Another relevant question is how the proposed experiments would be affected by using longer QD chains (which are already being pursued experimentally [61]).

In conclusion, although there are clearly challenges involved in experimental tests of non-Abelian physics with PMMs, we believe that this work has shown promising paths toward this goal.

ACKNOWLEDGMENTS

APPENDIX A: FUSION-PROTOCOL OUTCOME

Here, we show that the outcome of the fusion protocol suggested in Sec. VI C is 50-50 regardless of the weight $\zeta_{A,B}$ of the outer MBSs $\tilde{\gamma}_{A,B}$—mainly localized on AL and BR—on the inner QDs AR and BL (cf. Fig. 5). We consider the even-parity sector similarly to the main text. For an operation that is diabatic with respect to the ground-state splitting but adiabatic with respect to excited states, the probabilities for the fusion outcomes are given by the matrix elements

$$P_{n_A n_B} = |\langle e_\alpha e_\beta | n_A n_B \rangle|^2, \tag{A1}$$

where $|e_\alpha e_\beta\rangle$ is taken to be the ground state for the two coupled PMM systems modeled by the Hamiltonian given in Eq. (28) and $|n_A n_B\rangle$ correspond to the (almost) degenerate ground state for the uncoupled systems, right after step (ii) of the fusion protocol ($n_A, n_B = e_A$ or o_A). $|e_\alpha e_\beta\rangle$ is annihilated by the fermions:

$$f_\alpha = \frac{1}{2}\gamma_A + \frac{i}{2}\gamma_B, \quad f_\beta = \frac{1}{2}\tilde{\gamma}_A - \frac{i}{2}\tilde{\gamma}_B, \tag{A2}$$

which can be easily checked using the final result of this section. $|e_A e_B\rangle$ is annihilated by the fermions:

$$f_A = \frac{1}{2}\gamma_A + \frac{i}{2}\tilde{\gamma}_A, \quad f_B = \frac{1}{2}\gamma_B + \frac{i}{2}\tilde{\gamma}_B. \tag{A3}$$

We can read off the probabilities in Eq. (A1) by writing the ground state of the coupled systems in the basis $|n_A n_B\rangle$. The eigenvalues of Eq. (28) at the sweet spot ($\xi_+ = 0$) are

$$v_\pm = \pm \frac{\lambda_{AB}}{2}(1 - \zeta_A \zeta_B), \tag{A4}$$

with the corresponding normalized eigenvectors

$$V_\pm = \frac{1}{\sqrt{2}}\begin{pmatrix} 1 \\ \pm i \end{pmatrix}. \tag{A5}$$

The ground state can be written as

$$|e_\alpha e_\beta\rangle = \frac{1}{\sqrt{2}}[|e_A e_B\rangle - i|o_A o_B\rangle] \tag{A6}$$

and $P_{ee} = P_{oo} = 1/2$ for any $\zeta_{A,B}$. The fusion outcome is thus independent of the values of $\zeta_{A,B}$ and thus of the MP of the PMM systems. Although Eq. (28) is derived for a real and positive λ_{AB}, the conclusion is more general and is also valid for a complex λ_{AB}.

APPENDIX B: QUANTUM DOT READOUT FOR THE MEASUREMENT-BASED BRAIDING PROTOCOL

In this appendix, we give the details on how to calculate the projective measurements done by the readout QD U for the measurement-based braiding. The Hamiltonian is analogous to Eq. (30) and the QD U electron is described by the operator $d_U = (\gamma_U + i\tilde{\gamma}_U)/2$. Writing this in first-quantized form in the Majorana basis $\{\gamma_U, \tilde{\gamma}_U, \gamma_A, \tilde{\gamma}_A, \gamma_C, \tilde{\gamma}_C\}$, the Hamiltonian becomes (up to a constant)

$$H = \frac{i|\lambda_{AU}|}{2}\begin{pmatrix} 0 & \bar{\omega}_U & 0 & \zeta_A & \lambda\sin(\phi) & \zeta_C\lambda\cos(\phi) \\ -\bar{\omega}_U & 0 & -1 & 0 & -\lambda\cos(\phi) & \zeta_C\lambda\sin(\phi) \\ 0 & 1 & 0 & 0 & 0 & 0 \\ -\zeta_A & 0 & 0 & 0 & 0 & 0 \\ -\lambda\sin(\phi) & \lambda\cos(\phi) & 0 & 0 & 0 & 0 \\ -\zeta_C\lambda\cos(\phi) & -\zeta_C\lambda\sin(\phi) & 0 & 0 & 0 & 0 \end{pmatrix}, \tag{B1}$$

where $\bar{\omega}_U = \omega_U/|\lambda_{AU}|$ with ω_U the orbital energy of QD U, $\lambda = |\lambda_{CU}/\lambda_{AU}|$, and $\phi = \arg(\lambda_{CU}/\lambda_{AU})$. The two linear combinations of Majorana modes that couple to QD U are as follows:

$$\begin{aligned} a &= \zeta_A\tilde{\gamma}_A + \lambda\sin(\phi)\gamma_C + \zeta_C\lambda\cos(\phi)\tilde{\gamma}_C, \\ b &= \gamma_A + \lambda\cos(\phi)\gamma_C - \zeta_C\lambda\sin(\phi)\tilde{\gamma}_C. \end{aligned} \tag{B2}$$

After orthonormalization of these two vectors, we have that the fermion, the parity of which is read out by QD U, is given, in Majorana representation, by $f_U^{\text{read}} = (\gamma_U^{\text{read}} + i\tilde{\gamma}_U^{\text{read}})/2$ where

$$\gamma_U^{\text{read}} = (a - xb)\frac{\zeta_C^2\lambda^2\sin^2(\phi) + \lambda^2\cos^2(\phi) + 1}{\left(\zeta_A^2 + \lambda^2\sin^2(\phi)\right)\left(\zeta_C^2\lambda^2\sin^2(\phi) + 1\right) + \lambda^2\cos^2(\phi)\left(\zeta_A^2 + 2\zeta_C^2\lambda^2\sin^2(\phi) + \zeta_C^2\right) + \zeta_C^2\lambda^4\cos^4(\phi)},$$

$$\tilde{\gamma}_U^{\text{read}} = \frac{b}{\sqrt{1 + \lambda^2(\zeta_C^2\sin^2(\phi) + \cos^2(\phi))}},$$

$$x = \frac{\lambda^2\sin(\phi)\cos(\phi)(1 - \zeta_C^2)}{1 + \lambda^2(\zeta_C^2\sin^2(\phi) + \cos^2(\phi))}.$$

$$(B3)$$

The parity being projected by the measurement is thus

$$p_U = i\gamma_U^{\text{read}}\tilde{\gamma}_U^{\text{read}}. \tag{B4}$$

We note that for the case of perfect PMMs, $\zeta_A = \zeta_C = 0$, one obtains $\gamma_U^{\text{read}} \propto -\lambda\sin(\phi)\cos(\phi)\gamma_A + \sin(\phi)\gamma_C$ and $\tilde{\gamma}_U^{\text{read}} \propto \gamma_A + \lambda\cos(\phi)\gamma_C$. This means that $i\gamma_U^{\text{read}}\tilde{\gamma}_U^{\text{read}} \propto i\gamma_A\gamma_C$ as expected, independent of λ and ϕ.

When performing the calculations of the results of the braiding protocol, we define the fermion operators, $d_s = (\gamma_s + i\tilde{\gamma}_s)/2$, with $s = A, B, C$. These operators then act on the Fock basis states $|n_A n_C n_B\rangle$, which allows us to write the matrices for the various projectors.

[1] F. Wilczek, Majorana returns, Nat. Phys. **5**, 614 (2009).

[2] J. Alicea, New directions in the pursuit of Majorana fermions in solid state systems, Rep. Prog. Phys. **75**, 076501 (2012).

[3] M. Leijnse and K. Flensberg, Introduction to topological superconductivity and Majorana fermions, Semicond. Sci. Technol. **27**, 124003 (2012).

[4] R. Aguado, Majorana quasiparticles in condensed matter, Riv. Nuovo Cimento **40**, 523 (2017).

[5] C. W. J. Beenakker, Search for non-Abelian Majorana braiding statistics in superconductors, SciPost Phys. Lect. Notes **1**, 15 (2020).

[6] C. Nayak, S. H. Simon, A. Stern, M. Freedman, and S. Das Sarma, Non-Abelian anyons and topological quantum computation, Rev. Mod. Phys. **80**, 1083 (2008).

[7] S. Das Sarma, M. Freedman, and C. Nayak, Majorana zero modes and topological quantum computation, npj Quantum Inf. **1**, 15001 (2015).

[8] V. Lahtinen and J. K. Pachos, A short introduction to topological quantum computation, SciPost Phys. **3**, 021 (2017).

[9] P. Marra, Majorana nanowires for topological quantum computation, J. Appl. Phys. **132**, 231101 (2022).

[10] A. Y. Kitaev, Unpaired Majorana fermions in quantum wires, Phys. Usp. **44**, 131 (2001).

[11] R. M. Lutchyn, J. D. Sau, and S. Das Sarma, Majorana fermions and a topological phase transition in semiconductor-superconductor heterostructures, Phys. Rev. Lett. **105**, 077001 (2010).

[12] Y. Oreg, G. Refael, and F. von Oppen, Helical liquids and Majorana bound states in quantum wires, Phys. Rev. Lett. **105**, 177002 (2010).

[13] S. Nadj-Perge, I. K. Drozdov, B. A. Bernevig, and A. Yazdani, Proposal for realizing Majorana fermions in chains of magnetic atoms on a superconductor, Phys. Rev. B **88**, 020407(R) (2013).

[14] M. Hell, M. Leijnse, and K. Flensberg, Two-dimensional platform for networks of Majorana bound states, Phys. Rev. Lett. **118**, 107701 (2017).

[15] F. Pientka, A. Keselman, E. Berg, A. Yacoby, A. Stern, and B. I. Halperin, Topological superconductivity in a planar Josephson junction, Phys. Rev. X **7**, 021032 (2017).

[16] S. Vaitiekėnas, G. W. Winkler, B. van Heck, T. Karzig, M.-T. Deng, K. Flensberg, L. I. Glazman, C. Nayak, P. Krogstrup, R. M. Lutchyn, and C. M. Marcus, Flux-induced topological superconductivity in full-shell nanowires, Science **367**, 6485 (2020).

[17] K. Flensberg, F. von Oppen, and A. Stern, Engineered platforms for topological superconductivity and Majorana zero modes, Nat. Rev. Mater. **6**, 944 (2021).

[18] V. Mourik, K. Zuo, S. M. Frolov, S. R. Plissard, E. P. A. M. Bakkers, and L. P. Kouwenhoven, Signatures of Majorana fermions in hybrid superconductor-semiconductor nanowire devices, Science **336**, 1003 (2012).

[19] M. T. Deng, C. L. Yu, G. Y. Huang, M. Larsson, P. Caroff, and H. Q. Xu, Anomalous zero-bias conductance peak in a Nb-InSb nanowire-Nb hybrid device, Nano Lett. **12**, 6414 (2012).

[20] A. D. K. Finck, D. J. Van Harlingen, P. K. Mohseni, K. Jung, and X. Li, Anomalous modulation of a zero-bias peak in a hybrid nanowire-superconductor device, Phys. Rev. Lett. **110**, 126406 (2013).

[21] S. Nadj-Perge, I. K. Drozdov, J. Li, H. Chen, S. Jeon, J. Seo, A. H. MacDonald, B. A. Bernevig, and A. Yazdani, Observation of Majorana fermions in ferromagnetic atomic chains on a superconductor, Science **346**, 602 (2014).

[22] M. T. Deng, S. Vaitiekėnas, E. B. Hansen, J. Danon, M. Leijnse, K. Flensberg, J. Nygård, P. Krogstrup, and C. M. Marcus, Majorana bound state in a coupled quantum-dot hybrid-nanowire system, Science **354**, 1557 (2016).

[23] F. Nichele, A. C. C. Drachmann, A. M. Whiticar, E. C. T. O'Farrell, H. J. Suominen, A. Fornieri, T. Wang, G. C. Gardner, C. Thomas, A. T. Hatke, P. Krogstrup, M. J. Manfra, K. Flensberg, and C. M. Marcus, Scaling of

Majorana zero-bias conductance peaks, Phys. Rev. Lett. **119**, 136803 (2017).

[24] R. M. Lutchyn, E. P. Bakkers, L. P. Kouwenhoven, P. Krogstrup, C. M. Marcus, and Y. Oreg, Majorana zero modes in superconductor-semiconductor heterostructures, Nat. Rev. Mater. **3**, 52 (2018).

[25] A. Fornieri, A. M. Whiticar, F. Setiawan, E. Portolés, A. C. C. Drachmann, A. Keselman, S. Gronin, C. Thomas, T. Wang, R. Kallaher, G. C. Gardner, E. Berg, M. J. Manfra, A. Stern, C. M. Marcus, and F. Nichele, Evidence of topological superconductivity in planar Josephson junctions, Nature **569**, 89 (2019).

[26] H. Ren, F. Pientka, S. Hart, A. T. Pierce, M. Kosowsky, L. Lunczer, R. Schlereth, B. Scharf, E. M. Hankiewicz, L. W. Molenkamp, B. I. Halperin, and A. Yacoby, Topological superconductivity in a phase-controlled Josephson junction, Nature **569**, 93 (2019).

[27] M. Aghaee *et al.*, (Microsoft Quantum), InAs-Al hybrid devices passing the topological gap protocol, Phys. Rev. B **107**, 245423 (2023).

[28] A. Yazdani, F. von Oppen, B. I. Halperin, and A. Yacoby, Hunting for Majoranas, Science **380**, 6651 (2023).

[29] E. Prada, P. San-Jose, and R. Aguado, Transport spectroscopy of *NS* nanowire junctions with Majorana fermions, Phys. Rev. B **86**, 180503(R) (2012).

[30] G. Kells, D. Meidan, and P. W. Brouwer, Near-zero-energy end states in topologically trivial spin-orbit coupled superconducting nanowires with a smooth confinement, Phys. Rev. B **86**, 100503(R) (2012).

[31] J. Liu, A. C. Potter, K. T. Law, and P. A. Lee, Zero-bias peaks in the tunneling conductance of spin-orbit-coupled superconducting wires with and without Majorana end-states, Phys. Rev. Lett. **109**, 267002 (2012).

[32] J. Cayao, E. Prada, P. San-Jose, and R. Aguado, SNS junctions in nanowires with spin-orbit coupling: Role of confinement and helicity on the subgap spectrum, Phys. Rev. B **91**, 024514 (2015).

[33] C.-X. Liu, J. D. Sau, T. D. Stanescu, and S. Das Sarma, Andreev bound states versus Majorana bound states in quantum dot-nanowire-superconductor hybrid structures: Trivial versus topological zero-bias conductance peaks, Phys. Rev. B **96**, 075161 (2017).

[34] C. Moore, C. Zeng, T. D. Stanescu, and S. Tewari, Quantized zero-bias conductance plateau in semiconductor-superconductor heterostructures without topological Majorana zero modes, Phys. Rev. B **98**, 155314 (2018).

[35] C. Reeg, O. Dmytruk, D. Chevallier, D. Loss, and J. Klinovaja, Zero-energy Andreev bound states from quantum dots in proximitized Rashba nanowires, Phys. Rev. B **98**, 245407 (2018).

[36] O. A. Awoga, J. Cayao, and A. M. Black-Schaffer, Supercurrent detection of topologically trivial zero-energy states in nanowire junctions, Phys. Rev. Lett. **123**, 117001 (2019).

[37] A. Vuik, B. Nijholt, A. R. Akhmerov, and M. Wimmer, Reproducing topological properties with quasi-Majorana states, SciPost Phys. **7**, 61 (2019).

[38] H. Pan and S. Das Sarma, Physical mechanisms for zero-bias conductance peaks in Majorana nanowires, Phys. Rev. Res. **2**, 013377 (2020).

[39] E. Prada, P. San-Jose, M. W. A. de Moor, A. Geresdi, E. J. H. Lee, J. Klinovaja, D. Loss, J. Nygård, R. Aguado, and L. P. Kouwenhoven, From Andreev to Majorana bound states in hybrid superconductor-semiconductor nanowires, Nat. Rev. Phys. **2**, 575 (2020).

[40] R. Hess, H. F. Legg, D. Loss, and J. Klinovaja, Local and nonlocal quantum transport due to Andreev bound states in finite Rashba nanowires with superconducting and normal sections, Phys. Rev. B **104**, 075405 (2021).

[41] C. Janvier, L. Tosi, L. Bretheau, Ç. Ö. Girit, M. Stern, P. Bertet, P. Joyez, D. Vion, D. Esteve, M. F. Goffman, H. Pothier, and C. Urbina, Coherent manipulation of Andreev states in superconducting atomic contacts, Science **349**, 1199 (2015).

[42] M. Hays, G. de Lange, K. Serniak, D. J. van Woerkom, D. Bouman, P. Krogstrup, J. Nygård, A. Geresdi, and M. H. Devoret, Direct microwave measurement of Andreev-bound-state dynamics in a semiconductor-nanowire Josephson junction, Phys. Rev. Lett. **121**, 047001 (2018).

[43] M. Hays, V. Fatemi, D. Bouman, J. Cerrillo, S. Diamond, K. Serniak, T. Connolly, P. Krogstrup, J. Nygård, A. Levy Yeyati, A. Geresdi, and M. H. Devoret, Coherent manipulation of an Andreev spin qubit, Science **373**, 430 (2021).

[44] M. Hays, V. Fatemi, K. Serniak, D. Bouman, S. Diamond, G. de Lange, P. Krogstrup, J. Nygård, A. Geresdi, and M. H. Devoret, Continuous monitoring of a trapped superconducting spin, Nat. Phys. **16**, 1103 (2020).

[45] J. D. Sau and S. Das Sarma, Realizing a robust practical Majorana chain in a quantum-dot-superconductor linear array, Nat. Commun. **3**, 964 (2012).

[46] M. Leijnse and K. Flensberg, Parity qubits and poor man's Majorana bound states in double quantum dots, Phys. Rev. B **86**, 134528 (2012).

[47] I. C. Fulga, A. Haim, A. R. Akhmerov, and Y. Oreg, Adaptive tuning of Majorana fermions in a quantum dot chain, New J. Phys. **15**, 045020 (2013).

[48] P. Recher, E. V. Sukhorukov, and D. Loss, Andreev tunneling, Coulomb blockade, and resonant transport of nonlocal spin-entangled electrons, Phys. Rev. B **63**, 165314 (2001).

[49] L. Hofstetter, S. Csonka, J. Nygård, and C. Schönenberger, Cooper pair splitter realized in a two-quantum-dot Y-junction, Nature **461**, 960 (2009).

[50] L. G. Herrmann, F. Portier, P. Roche, A. L. Yeyati, T. Kontos, and C. Strunk, Carbon nanotubes as Cooper-pair beam splitters, Phys. Rev. Lett. **104**, 026801 (2010).

[51] J. Schindele, A. Baumgartner, and C. Schönenberger, Near-unity Cooper pair splitting efficiency, Phys. Rev. Lett. **109**, 157002 (2012).

[52] C.-X. Liu, G. Wang, T. Dvir, and M. Wimmer, Tunable superconducting coupling of quantum qots via Andreev bound states in semiconductor-superconductor nanowires, Phys. Rev. Lett. **129**, 267701 (2022).

[53] A. Tsintzis, R. S. Souto, and M. Leijnse, Creating and detecting poor man's Majorana bound states in interacting quantum dots, Phys. Rev. B **106**, L201404 (2022).

[54] S. V. Aksenov, A. O. Zlotnikov, and M. S. Shustin, Strong Coulomb interactions in the problem of Majorana modes

in a wire of the nontrivial topological class BDI, Phys. Rev. B **101**, 125431 (2020).

[55] N. Sedlmayr and C. Bena, Visualizing Majorana bound states in one and two dimensions using the generalized Majorana polarization, Phys. Rev. B **92**, 115115 (2015).

[56] N. Sedlmayr, J. M. Aguiar-Hualde, and C. Bena, Majorana bound states in open quasi-one-dimensional and two-dimensional systems with transverse Rashba coupling, Phys. Rev. B **93**, 155425 (2016).

[57] G. Wang, T. Dvir, G. P. Mazur, C.-X. Liu, N. van Loo, S. L. D. ten Haaf, A. Bordin, S. Gazibegovic, G. Badawy, E. P. A. M. Bakkers, M. Wimmer, and L. P. Kouwenhoven, Singlet and triplet Cooper pair splitting in hybrid superconducting nanowires, Nature **612**, 448 (2022).

[58] T. Dvir, G. Wang, N. van Loo, C.-X. Liu, G. P. Mazur, A. Bordin, S. L. D. ten Haaf, J.-Y. Wang, D. van Driel, F. Zatelli, X. Li, F. K. Malinowski, S. Gazibegovic, G. Badawy, E. P. A. M. Bakkers, M. Wimmer, and L. P. Kouwenhoven, Realization of a minimal Kitaev chain in coupled quantum dots, Nature **614**, 445 (2023).

[59] Q. Wang, S. L. D. ten Haaf, I. Kulesh, D. Xiao, C. Thomas, M. J. Manfra, and S. Goswami, Triplet correlations in Cooper pair splitters realized in a two-dimensional electron gas, Nat. Commun. **14**, 4876 (2023).

[60] A. Bordin, G. Wang, C.-X. Liu, S. L. D. ten Haaf, N. van Loo, G. P. Mazur, D. Xu, D. van Driel, F. Zatelli, S. Gazibegovic, G. Badawy, E. P. A. M. Bakkers, M. Wimmer, L. P. Kouwenhoven, and T. Dvir, Tunable crossed Andreev reflection and elastic cotunneling in hybrid nanowires, Phys. Rev. X **13**, 031031 (2023).

[61] A. Bordin, X. Li, D. van Driel, J. C. Wolff, Q. Wang, S. L. D. ten Haaf, G. Wang, N. van Loo, L. P. Kouwenhoven, and T. Dvir, Crossed Andreev reflection and elastic co-tunneling in a three-site Kitaev chain nanowire device, arXiv:2306.07696 (2023).

[62] F. Zatelli *et al.*, Robust poor man's Majorana zero modes using Yu-Shiba-Rusinov states, arXiv:2311.03193 (2023).

[63] S. L. D. ten Haaf *et al.*, Engineering Majorana bound states in coupled quantum dots in a two-dimensional electron gas, arXiv:2311.03208 (2023).

[64] J. Cayao and A. M. Black-Schaffer, Distinguishing trivial and topological zero-energy states in long nanowire junctions, Phys. Rev. B **104**, L020501 (2021).

[65] C. Zeng, G. Sharma, T. D. Stanescu, and S. Tewari, Feasibility of measurement-based braiding in the quasi-Majorana regime of semiconductor-superconductor heterostructures, Phys. Rev. B **102**, 205101 (2020).

[66] D. Liu, Z. Cao, X. Liu, H. Zhang, and D. E. Liu, Topological Kondo device for distinguishing quasi-Majorana and Majorana signatures, Phys. Rev. B **104**, 205125 (2021).

[67] H. Tian and C. Ren, Distinguishing Majorana and quasi-Majorana bound states in a hybrid superconductor-semiconductor nanowire with inhomogeneous potential barriers, Res. Phys. **26**, 104273 (2021).

[68] L. S. Ricco, V. K. Kozin, A. C. Seridonio, and I. A. Shelykh, Accessing the degree of Majorana nonlocality in a quantum dot-optical microcavity system, Sci. Rep. **12**, 1983 (2022).

[69] P. Marra and A. Nigro, Majorana/Andreev crossover and the fate of the topological phase transition in inhomogeneous nanowires, J. Phys.: Condens. Matter **34**, 124001 (2022).

[70] C. Zeng, G. Sharma, S. Tewari, and T. Stanescu, Partially separated Majorana modes in a disordered medium, Phys. Rev. B **105**, 205122 (2022).

[71] J. Gramich, A. Baumgartner, and C. Schönenberger, Andreev bound states probed in three-terminal quantum dots, Phys. Rev. B **96**, 195418 (2017).

[72] T. Ö. Rosdahl, A. Vuik, M. Kjaergaard, and A. R. Akhmerov, Andreev rectifier: A nonlocal conductance signature of topological phase transitions, Phys. Rev. B **97**, 045421 (2018).

[73] G. Ménard, G. L. R. Anselmetti, E. A. Martinez, D. Puglia, F. K. Malinowski, J. S. Lee, S. Choi, M. Pendharkar, C. J. Palmstrøm, K. Flensberg, C. M. Marcus, L. Casparis, and A. P. Higginbotham, Conductance-matrix symmetries of a three-terminal hybrid device, Phys. Rev. Lett. **124**, 036802 (2020).

[74] J. Danon, A. B. Hellenes, E. B. Hansen, L. Casparis, A. P. Higginbotham, and K. Flensberg, Nonlocal conductance spectroscopy of Andreev bound states: Symmetry relations and BCS charges, Phys. Rev. Lett. **124**, 036801 (2020).

[75] H. Pan, J. D. Sau, and S. Das Sarma, Three-terminal nonlocal conductance in Majorana nanowires: Distinguishing topological and trivial in realistic systems with disorder and inhomogeneous potential, Phys. Rev. B **103**, 014513 (2021).

[76] D. I. Pikulin *et al.*, Protocol to identify a topological superconducting phase in a three-terminal device, arXiv:2103.12217 (2021).

[77] D. J. Clarke, Experimentally accessible topological quality factor for wires with zero energy modes, Phys. Rev. B **96**, 201109(R) (2017).

[78] M.-T. Deng, S. Vaitiekėnas, E. Prada, P. San-Jose, J. Nygård, P. Krogstrup, R. Aguado, and C. M. Marcus, Nonlocality of Majorana modes in hybrid nanowires, Phys. Rev. B **98**, 085125 (2018).

[79] J. Alicea, Y. Oreg, G. Refael, F. von Oppen, and M. P. A. Fisher, Non-Abelian statistics and topological quantum information processing in 1D wire networks, Nat. Phys. **7**, 412 (2011).

[80] B. van Heck, A. R. Akhmerov, F. Hassler, M. Burrello, and C. W. J. Beenakker, Coulomb-assisted braiding of Majorana fermions in a Josephson junction array, New J. Phys. **14**, 035019 (2012).

[81] D. Aasen *et al.*, Milestones toward Majorana-based quantum computing, Phys. Rev. X **6**, 031016 (2016).

[82] M. Hell, J. Danon, K. Flensberg, and M. Leijnse, Time scales for Majorana manipulation using Coulomb blockade in gate-controlled superconducting nanowires, Phys. Rev. B **94**, 035424 (2016).

[83] K. Flensberg, Non-Abelian operations on Majorana fermions via single-charge control, Phys. Rev. Lett. **106**, 090503 (2011).

[84] S. Plugge, A. Rasmussen, R. Egger, and K. Flensberg, Majorana box qubits, New J. Phys. **19**, 012001 (2017).

[85] T. Karzig, C. Knapp, R. M. Lutchyn, P. Bonderson, M. B. Hastings, C. Nayak, J. Alicea, K. Flensberg, S. Plugge, Y. Oreg, C. M. Marcus, and M. H. Freedman, Scalable designs for quasiparticle-poisoning-protected topological quantum computation with Majorana zero modes, Phys. Rev. B **95**, 235305 (2017).

[86] M. I. K. Munk, J. Schulenborg, R. Egger, and K. Flensberg, Parity-to-charge conversion in Majorana qubit readout, Phys. Rev. Res. **2**, 033254 (2020).

[87] J. F. Steiner and F. von Oppen, Readout of Majorana qubits, Phys. Rev. Res. **2**, 033255 (2020).

[88] J. M. Elzerman, R. Hanson, L. H. W. van Beveren, B. Witkamp, L. M. K. Vandersypen, and L. P. Kouwenhoven, Single-shot read-out of an individual electron spin in a quantum dot, Nature **430**, 431 (2004).

[89] D. J. Reilly, C. M. Marcus, M. P. Hanson, and A. C. Gossard, Fast single-charge sensing with a rf quantum point contact, Appl. Phys. Lett. **91**, 162101 (2007).

[90] C. Barthel, D. J. Reilly, C. M. Marcus, M. P. Hanson, and A. C. Gossard, Rapid single-shot measurement of a singlet-triplet qubit, Phys. Rev. Lett. **103**, 160503 (2009).

[91] C. Volk, A. Chatterjee, F. Ansaloni, C. M. Marcus, and F. Kuemmeth, Fast charge sensing of Si/SiGe quantum dots via a high-frequency accumulation gate, Nano Lett. **19**, 5628 (2019).

[92] Y.-Y. Liu, S. Philips, L. Orona, N. Samkharadze, T. McJunkin, E. MacQuarrie, M. Eriksson, L. Vandersypen, and A. Yacoby, Radio-frequency reflectometry in silicon-based quantum dots, Phys. Rev. Appl. **16**, 014057 (2021).

[93] K. D. Petersson, C. G. Smith, D. Anderson, P. Atkinson, G. A. C. Jones, and D. A. Ritchie, Charge and spin state readout of a double quantum dot coupled to a resonator, Nano Lett. **10**, 2789 (2010).

[94] N. J. Lambert, A. A. Esmail, M. Edwards, F. A. Pollock, B. W. Lovett, and A. J. Ferguson, Quantum capacitance and charge sensing of a superconducting double dot, Appl. Phys. Lett. **109**, 112603 (2016).

[95] F. Vigneau, F. Fedele, A. Chatterjee, D. Reilly, F. Kuemmeth, M. F. Gonzalez-Zalba, E. Laird, and N. Ares, Probing quantum devices with radio-frequency reflectometry, Appl. Phys. Rev. **10**, 021305 (2023).

[96] S. Bravyi, Universal quantum computation with the $\nu = 5/2$ fractional quantum Hall state, Phys. Rev. A **73**, 042313 (2006).

[97] M. Hell, K. Flensberg, and M. Leijnse, Coupling and braiding Majorana bound states in networks defined in two-dimensional electron gases with proximity-induced superconductivity, Phys. Rev. B **96**, 035444 (2017).

[98] D. J. Clarke, J. D. Sau, and S. Das Sarma, Probability and braiding statistics in Majorana nanowires, Phys. Rev. B **95**, 155451 (2017).

[99] C. W. J. Beenakker, A. Grabsch, and Y. Herasymenko, Electrical detection of the Majorana fusion rule for chiral edge vortices in a topological superconductor, SciPost Phys. **6**, 022 (2019).

[100] T. Zhou, M. C. Dartiailh, W. Mayer, J. E. Han, A. Matos-Abiague, J. Shabani, and I. Žutić, Phase control of Majorana bound states in a topological X junction, Phys. Rev. Lett. **124**, 137001 (2020).

[101] T. Zhou, M. C. Dartiailh, K. Sardashti, J. E. Han, A. Matos-Abiague, J. Shabani, and I. Žutić, Fusion of Majorana bound states with mini-gate control in two-dimensional systems, Nat. Commun. **13**, 1738 (2022).

[102] R. S. Souto and M. Leijnse, Fusion rules in a Majorana single-charge transistor, SciPost Phys. **12**, 161 (2022).

[103] C.-X. Liu, H. Pan, F. Setiawan, M. Wimmer, and J. D. Sau, Fusion protocol for Majorana modes in coupled quantum dots, Phys. Rev. B **108**, 085437 (2023).

[104] D. A. Ivanov, Non-Abelian statistics of half-quantum vortices in p-wave superconductors, Phys. Rev. Lett. **86**, 268 (2001).

[105] P. Boross and A. Pályi, Braiding-based quantum control of a Majorana qubit built from quantum dots, arXiv:2305.08464 (2023).

[106] R. S. Souto, K. Flensberg, and M. Leijnse, Timescales for charge transfer based operations on Majorana systems, Phys. Rev. B **101**, 081407(R) (2020).

[107] S. Krøjer, R. S. Souto, and K. Flensberg, Demonstrating Majorana non-Abelian properties using fast adiabatic charge transfer, Phys. Rev. B **105**, 045425 (2022).

[108] P. Bonderson, M. Freedman, and C. Nayak, Measurement-only topological quantum computation, Phys. Rev. Lett. **101**, 010501 (2008).

[109] D. J. Clarke, J. D. Sau, and S. Tewari, Majorana fermion exchange in quasi-one-dimensional networks, Phys. Rev. B **84**, 035120 (2011).

[110] T. Karzig, F. Pientka, G. Refael, and F. von Oppen, Shortcuts to non-Abelian braiding, Phys. Rev. B **91**, 201102(R) (2015).

[111] D. Stepanenko, M. Rudner, B. I. Halperin, and D. Loss, Singlet-triplet splitting in double quantum dots due to spin-orbit and hyperfine interactions, Phys. Rev. B **85**, 075416 (2012).

[112] G. Kiršanskas, J. N. Pedersen, O. Karlström, M. Leijnse, and A. Wacker, QmeQ 1.0: An open-source PYTHON package for calculations of transport through quantum dot devices, Comput. Phys. Commun. **221**, 317 (2017).

[113] D. E. Liu, M. Cheng, and R. M. Lutchyn, Probing Majorana physics in quantum-dot shot-noise experiments, Phys. Rev. B **91**, 081405(R) (2015).

[114] D. E. Liu, A. Levchenko, and R. M. Lutchyn, Majorana zero modes choose Euler numbers as revealed by full counting statistics, Phys. Rev. B **92**, 205422 (2015).

[115] S. Smirnov, Majorana finite-frequency nonequilibrium quantum noise, Phys. Rev. B **99**, 165427 (2019).

[116] G.-H. Feng and H.-H. Zhang, Probing robust Majorana signatures by crossed Andreev reflection with a quantum dot, Phys. Rev. B **105**, 035148 (2022).

[117] S. Smirnov, Revealing universal Majorana fractionalization using differential shot noise and conductance in nonequilibrium states controlled by tunneling phases, Phys. Rev. B **105**, 205430 (2022).

[118] S. Smirnov, Majorana differential shot noise and its universal thermoelectric crossover, Phys. Rev. B **107**, 155416 (2023).

[119] Z. Cao, G. Zhang, H. Zhang, Y.-X. Liang, W.-X. He, K. He, and D. E. Liu, Differential current noise as an identifier of Andreev bound states that induce nearly quantized

conductance plateaus, Phys. Rev. B **108**, L121407 (2023).

[120] S. Smirnov, Majorana tunneling entropy, Phys. Rev. B **92**, 195312 (2015).

[121] E. Sela, Y. Oreg, S. Plugge, N. Hartman, S. Lüscher, and J. Folk, Detecting the universal fractional entropy of Majorana zero modes, Phys. Rev. Lett. **123**, 147702 (2019).

[122] S. Smirnov, Majorana entropy revival via tunneling phases, Phys. Rev. B **103**, 075440 (2021).

[123] S. Smirnov, Majorana ensembles with fractional entropy and conductance in nanoscopic systems, Phys. Rev. B **104**, 205406 (2021).

[124] C. Han, Z. Iftikhar, Y. Kleeorin, A. Anthore, F. Pierre, Y. Meir, A. K. Mitchell, and E. Sela, Fractional entropy of multichannel Kondo systems from conductance-charge relations, Phys. Rev. Lett. **128**, 146803 (2022).

[125] E. Prada, R. Aguado, and P. San-Jose, Measuring Majorana nonlocality and spin structure with a quantum dot, Phys. Rev. B **96**, 085418 (2017).

[126] M. Geier, S. Krøjer, F. von Oppen, C. M. Marcus, K. Flensberg, and P. W. Brouwer, Non-Abelian holonomy of Majorana zero modes coupled to a chaotic quantum dot, arXiv:2304.06754 (2023).

[127] G. Széchenyi and A. Pályi, Parity-to-charge conversion for readout of topological Majorana qubits, Phys. Rev. B **101**, 235441 (2020).

[128] J. Schulenborg, S. Krøjer, M. Burrello, M. Leijnse, and K. Flensberg, Detecting Majorana modes by readout of poisoning-induced parity flips, Phys. Rev. B **107**, L121401 (2023).

[129] G. Burkard, T. D. Ladd, A. Pan, J. M. Nichol, and J. R. Petta, Semiconductor spin qubits, Rev. Mod. Phys. **95**, 025003 (2023).